國立交通大學

材料科學與工程學系

奈米科技博士班

博士論文

應用奈米結構表面探討細胞介面的貼附行為與功能性表現

Application of nanostructured interface to estimate the cell behaviors and functional expression for biomedical engineering

研究生: 潘敘安

指導教授: 黃國華 教授

中華民國一０一年六月

應用奈米結構表面探討細胞介面的貼附行為與功能性表現

Application of nanostructured interface to estimate the cell behaviors and functional expression for biomedical engineering

研究生: 潘敘安　　Student: Hsu-An Pan

指導教授: 黃國華 教授　　Advisor: Guewha Steven Huang

國立交通大學

材料科學與工程學系奈米科技博士班

博士論文

A Thesis
Submitted to Graduate Program for Nanotechnology
Department of Materials Science and Engineering
College of Engineering
National Chiao Tung University
In partial Fulfillment of the Requirements
For the Degree of
Doctor of Philosophy
in
Materials Science and Engineering

June 2012
Hsinchu, Taiwan, Republic of China

中華民國一0一年六月

摘要

在細胞生長的過程中，細胞本身具有感知外在各式各樣的化學或物理信號並整合與分析這些外在環境訊息的能力，進而改變其細胞形態及生長行為模式。此外大多數細胞於偵測環境表面適於生長後，則開始進行貼附行為並表現該細胞的生長模式與型態變化，因此對於細胞貼附基質的特性研究將是發展細胞工程中重要的一環。目前在仿生基材的研究成果已廣泛應用於醫學領域，而最近的研究報告指出，微米結構化的表面具有模仿天然細胞外基質的特性，能夠促進細胞生長和分化，但細胞外基質是由微米與奈米結構所交織組成的天然結構表面，而目前細胞對奈米結構的反應與行為機制仍處於摸索階段。為了進一步研究微米級細胞對於奈米級結構表面的感知與行為反應，本研究利用直徑從10到200奈米的奈米點陣列探討各式不同類型的細胞型態與行為，以評估細胞對奈米尺度的反應。奈米點陣列以陽極氧化鋁為模板，製造於鍍上TaN的矽晶圓上，並濺鍍約 5奈米厚的白金層以提供一個同質性與良好的生物相容性表面。

為了探討微米級細胞與奈米級基材之間的作用反應，我們將觀察細胞如何透過貼附奈米結構基材，並展現其生長型態的變化與胞內的功能機轉，本研究中分為四個部分:

本論文研究第一部分主要探討利用系統化的奈米尺度點陣列，範圍從10奈米到200奈米的奈米點陣列，探討3T3纖維母細胞貼附行為與生長條件。我們發現以奈米點陣列的基材表面可能會誘導3T3纖維母細胞異常的凋亡。異常的細胞形態在培養於200奈米的點陣列24小時候被觸發，細胞自本體延展的偽足數目明顯的減少。在利用纖維連接蛋白與第一型膠原蛋白預塗層處理後，則可以有效預防奈米拓樸結構所引發的程序性細胞死亡，因此奈米結構觸發細胞異常凋亡的調控程序主要是透過Focal adhesion的形成。

在本論文研究的第二部分，利用Cardiomyoblast (H9c2)培養於直徑介於10和200 nm的奈米點陣列上進行觀察。我們發現H9c2細胞在50奈米的奈米點陣列上

具有廣泛的偽足延展與面積分佈，並具有極佳的增生能力。相對於大尺寸奈米點陣列，100奈米與200奈米則減少了53.7％和72.6％的細胞增生數目，並生成較少的貼附蛋白與細胞骨架。而細胞纖維化和心肌肥大相關基因在培養於100奈米的細胞基因表現分析中則具有顯著的提升，此外，在胞內蛋白質分析中，培養於50奈米的細胞則具有大量Vinculin與PAI-1蛋白表現。根據這些分析結果我們可以藉由調整奈米點的直徑，調節Cardiomyoblast的增生與相關功能性基因及蛋白質的表現。

在本論文的第三部分，我們運用分析系列尺度的奈米點結構對於成骨細胞在體外培養的反應，以提供牙根植體表面優化的策略與設計依據。在體外培養分析中，利用直徑範圍從10奈米到200奈米的點陣列進行對類成骨細胞(MG63)的細胞活性，自體凋亡，貼附行為以及細胞骨架組成進行評估。我們發現50奈米點陣列相對於平面結構增加了44％的細胞活性，減少2.7％細胞凋亡程度，並促進30％的肌動蛋白纖維束增長，同時增加了73％的細胞貼附程度，此外也加強了約50%的細胞礦化程度。在本研究中，我們應用類成骨細胞模型系統可以評估出最佳的奈米點結構表面，有利於改善牙根植體表面的設計以達到最佳的生物相容性。

在本論文的最後一部分，我們製備了一個具有快速分析並調控癌細胞的增生，凋亡，侵襲能力以及胞內骨架重組的奈米表面平台。透過從一個平面至10奈米，50奈米，100奈米和200奈米點陣列所組成的奈米點矩陣，我們能夠有效區分出子宮頸癌細胞HeLa與較後期的C33A的細胞侵襲能力。在各類型的卵巢癌細胞株（ES2, PA-1, TOV-112D, TOV-21G）體外培養分析中，**癌細胞本身的類型與相關期數也表現出相對差異性的生長模式**。因此透過簡單與低成本的製造過程，我們所建製的奈米點矩陣平台可有效用於評估各類型細胞生長的基本特徵，並能夠區分不同期數與類型的癌細胞，同時也可以提供人工植入物的基本設計參數，因此本研究中的奈米點陣列平台將可作為一個方便且快速的癌症檢測工具。

Abstract

Cells sense and respond to a wide range of external signals, both chemical and physical. Extra-cellular information penetrates cell membrane, transmits through cytoskeleton, affects muscle genes expression, and alters the cytoskeleton organization. Eventually, cell morphology is changed leading to better growth or death. The modification of biomimetic substratum has been wildly used to study the effects of bio-nano interface on cell adhesion and subsequent growth and function. Micro-structures direct cell migration; however the cellular response to nanostructures is yet to be explored. In the current study, nanotopology is defined by nanodot arrays with dot diameters ranging from 10 to 200 nm. The nanodot arrays were fabricated by AAO processing on TaN-coated wafers. A thin layer of platinum, 5 nm in thickness, was sputtered onto the structure to provide a well biocompatible and homogeneous surface.

The defined nanostructures utilized in this study significantly facilitate our understanding of cell-nanosubstratum interactions. Our results were separated into four sections in this dissertation.

In the first part of this dissertation, nanodot arrays ranging from 10 nm to 200 nm were utilized to study the cellular adhesion behavior and growth condition in 3T3 fibroblasts. We found nanotopography, in the form of nanodot arrays, induced an apoptosis-like abnormality for cultured 3T3 fibroblast cells. Abnormality was triggered after as few as 24 hours of incubation on a 200 nm dot array. The number of filopodia extended from the cell bodies was lower for the abnormal cells. Pre-coatings of fibronectin or collagen type I promoted cellular anchorage and prevented the nanotopography-induced programmed cell death. The occurrence of the abnormality was mediated by the formation of focal adhesions.

In the second part of this dissertation, the cardiomyoblasts H9c2 were cultured on nanodot arrays. On the 50 nm nanodot arrays H9c2 showed maximum attachment and proliferation with largest cell area and extended lamellipodia. In contrast, 53.7% and 72.6% reductions of growth were observed on the 100- and 200 nm nanodot arrays. Immunostaining indicated that nanodots smaller than 50 nm induced cell adhesion and cytoskeleton organization. Expression of genes associated with fibrosis and hypertrophy was up-regulated in cells grown on 100 nm nanodots. The analysis of protein expression showed high levels of expression for vinculin and plasminogen activator inhibitor-1 for cells cultured on 50 nm nanodots. By adjusting the diameter of the nanodots, we could modulate the growth and expression of function-related genes and proteins in cardiomyoblasts.

In the third part of this dissertation, a strategy was proposed for the topologic design of dental implants based on the *in vitro* survey of optimized nanodot structures. An *in vitro* survey was performed using nanodot arrays with dot diameters ranging from 10 nm to 200 nm. Cell viability, apoptosis, cell adhesion, and cytoskeletal organization of MG63 osteoblasts were evaluated. Nanodots with a diameter of approximately 50 nm enhanced 44 % cell viability, minimized apoptosis to 2.7 %, promoted 30 % increase in actin filament bundles, and maximized cell adhesion with a 73 % increase in focal adhesions. Enhancement of ~50 % in mineralization was observed. We showed optimization for the biocompatibility of dental implants using nano-structures/MG 63 osteoblasts model system, providing a topologic approach beneficial for the design of dental implants.

In the last part of this dissertation, different sizes of nanodot arrays were integrated into a nanodevice for rapid modulation of proliferation, apoptosis, invasive ability, and cytoskeletal reorganization for cancer cells. The nanodevice composed of a matrix of nine nanodot arrays ranging from a flat surface to 10 nm, 50 nm, 100 nm, and 200 nm arrays. The invasive ability of HELA versus later-staged C33A cells was distinguished. Ovarian cancer cell lines (ES2, PA-1, TOV-112D, and TOV-21G) exhibited differential growth parameters that are associated with cell type, grade, and stage. We have established a platform that can be used to assess basic parameters of cell growth. The device is capable of distinguishing among cancer cell lines at various stages and also provides basic design parameters for artificial implants. Our device will serve as a convenient and fast tool for tissue engineering and cancer treatment.

致謝

阿潘哥~終於沒有成為宅男，順利畢業囉!!

交通大學!!我作夢都沒想到我會有機會到這裡完成我的博士學位,首先非常感謝黃國華老師提供我最大的幫助以及最重要的建議與指導,讓我能夠更深入了解科學的涵意與研究的精神，讓我能在如此豐富資源的環境下專心完成我的論文。實驗過程雖然一路上跌跌撞撞，但多虧有師母洪孟燕 女士積極的指導與照顧，讓我在生活規劃與為人處事方面精進許多,也得以順利完成這本論文,也才能有今日的Dr.潘。此外非常感謝實驗室大大小小的夥伴們，大勳學長與阿亮老師謝謝你們讓我學到如何維持互動的帶人技巧與實驗設計邏輯。另外，實驗室所有的弟弟妹妹們，超級感謝你們這些日子無論在實驗或生活上給予我許多的幫助，以及傾聽我一張嘴的碎碎念，陪伴我走過無數的低潮期，並帶給我許多歡樂的回憶，我想沒有你們，我的博士班生活是黑白的，敬大家~我的保肝丸!!讓我有如此酸甜苦辣、永生難忘的彩色人生。最後感謝口試委員陳俊勳院長、歐陽盟教授、吳啟瑞教授、林立偉教授對我論文的審閱與意見指導。

老爸~老媽~你兒子畢業啦!!

感謝你們生了一個我這樣的兒子，我很滿意你們給我的基因~MAGIC!，這些年讓你們操心了，還得時常容忍我因壓力而造成的情緒化脾氣，爸媽、老姊 ~謝謝你們 ^ε^

叙安 謹誌 2012.06.26

TABLE OF CONTENTS

LIST OF TABLES

LIST OF FIGURES

1. Introduction

Environmental sensing by living cells displays mangy features that are usually ascribed to chemical or physical interface between cell and surface. In recent years, scientists have great interests about the interaction between cells and the underlying ligands such as extracellular matrix (ECM). Cells detect and respond to the specific ligands and the spatial organization of the scaffoldings. The ECM consists of collagen and elastin fibers of 10–300 nm diameters intertwined into a landscape of peaks, valleys, and pores [1]. Since ECM contains structures from micro-scale down to nano-scale, it is hypothesized that cells respond to both micro-structure and nano-structure. They have found that topography of micrometric scale could affect cellular gene expression, adhesion, migration, proliferation, and differentiation. Nowadays relying on progressive nanotechnology, numerous nanostructures have been developed and applied to the field of cell research. It's believed that nanostructure is more close to the actual scale of the ligands interacted with cells.

1.1 Micron-scale surface topography

The cell adhesion–mediated sensing of the microtopographical environment displays a critical role in cellular processes including cell morphology [2], focal adhesion [3-4], proliferation [5-6], migration [7-9] and differentiation [10]. Recently, a growing number of studies have shown that introducing a microtopography to the substrate of both two and three dimensional cell culture systems promote cell adhesion [3-4]. Micro-scaled landscapes have been fabricated to direct growth of cultured cells. When cultured on ridges and grooves of nanoscale dimensions, cells migrated more extensively to the ridges than into the grooves. The cells' shapes were aligned and extended in the direction of the grooves [4, 11]. It has been shown that a three-dimensional micro-structure that mimics ECM provides an environment for the in vivo growth of cells. Although cellular response to microtopography has been extensivly investigated, the nanotopography that cells respond to and the molecular apparatus that senses and transmit the spatial signal from the membrane to the nucleus are not clearly defined at the present time.

1.2 Biomimetics and nanotopography

The recapitulation of natural cellular environments can be achieved at the nanoscale [12]. The three-dimensionality and nanostructure architecture of the ECM may represent essential element in signal transduction pathways and cellular physiology. Nanoscaled modification of a surface could contribute to the mimicry of cellular environments. For example, the structure of the epithelial basement membrane contains pores approximating 70–100 nm [13]. It is suggested that the surface roughness of bone is approximately 32 nm making it within the nanoscale range of current nanotechnology investigations [14-17]. The surface topology at the nanoscale encodes information that directs cell behaviour [18]. Increasing evidence indicates that physical structures affect cell behaviour by providing scaffolds and interacting with the integrins on the cell membrane. Nanoscale texture generated through the deposition of nanocoatings may be useful to improve biocompatibility because surface topography can promote vascular smooth muscle cell and endothelial cell adherence and proliferation [19-20]. In vivo, cells live in environment with specific three-dimensional features of micro- and nanoscale. The ECM that cells interact with displays nano-scaled topography [21-22]. Nanotopographies could control cell growth and function via mechanical mechanisms. The nanostructures such as nanopillar, nanowire, nanodot, and nanoflower have reported in promoting cell growth and functions [23-26].

Many studies indicate that various nanostructured surfaces can influence the *in vitro* adhesion [27-29], morphology [30-32], proliferation [33], and gene expression [34] of different cell types. The cellular response to a nanostructured substrate depends on the size arrangement of the topographic features and cell type [35-36]. Cell adhesion and spreading were severely impaired on nanotube layers with tube diameters larger than 50 nm, resulting in dramatically reduced cellular activity and high degrees of programmed cell death. The 15 nm-spaced TiO2 nanotubes optimizes cell adhesion and differentiation [37]. Highly ordered surfaces of 120 nm nanopores significantly reduce cell adhesion by modulating filopodia formation and preventing focal adhesion formation [38-39]. It demonstrates the migration rates of human vascular endothelial cell to the ridge and groove topographic cues [40]. Nanofibers induce faster cellular migration and may be useful as biomedical implant to induce wound closure and tissue regeneration [41]. The correlation of gene expression regulated by nanotopography that controls cell growth and function remains to be explored. These results may be changed in physical properties including enhanced magnetic, catalytic, optical, electrical, mechanical, and biological properties when compared to conventional formulations of the same material [42].

1.3 Nanotopography alters cellular responses

Surface nanotopography alters cell behaviors and affects cell interactions when compared to conventional sized topography [43-45]. Different physical relationships exist between cells and nano- vs cell and micron-scale surface features. Nanotopography affects cellular behavior in a wide range of cell types including osteoblasts, epithelial cells, fibroblasts, myocytes, and stem cell [12]. Nanoscale features can increase adherent cell proliferation [46]. The topographical surface alters osteoblastic attachment, proliferation, differentiation, and matrix production [47-48].

Webster and colleagues [49] also observed increased osteoblast proliferation on nanoscale materials (alumina, titania, and calcium phosphate). Osteoblasts grown on a fibrous matrix composed of multiwalled carbon nanofibers (100 nm in diameter) exhibited increased proliferation compared to those grown on flat glass surfaces [50-51]. The use of nanostructures presents an opportunity to positively and negatively modulate cell adhesion and spreading. Cells that adhere to nanotopography may possess altered motility. Recent reports demonstrated that fibroblasts and mesenchymal stem cell (MSC) motility varied remarkably across a small range of nanostructures [35, 52].

An interesting feature of the nanoscale topographic surfaces is the selectivity for cell adhesion. Several investigators have demonstrated the relative diminution of fibroblast adhesion compared to osteoblast adhesion when nano- and micron-structured surfaces were evaluated [51, 53]. Nanotopography-induced cellular response has been explored using nanoislands [17]. Nanoislands were fabricated through varying the polymer blend and allowing spontaneous demixing [54]. Strong influences on the formation of focal adhesions, reorganization of cytoskeleton, and change in the mobility were observed [55]. The cells manage an initial fast organization of the cytoskeleton in reaction to the islands [56]. It has been observed that 13 nm-high islands induce cell spreading and proliferation, while 160 nm islands retard the attachment of filopodia. A gene expression study using a microarray indicates the down regulation of genes associated with the cytoskeleton for cells grown on 95 nm deep nanoislands. The cells responded to the islands with broad gene up-regulation, notably those involved in cell signaling, proliferation, the cytoskeleton, and the production of extracellular matrix protein [57].

1.4 Application of nanotopologic surface for implant

1.4.1 Design of stent for cardiovascular implant

Control of cell proliferation, adhesion, and function at the bio-surface interface is essential for the long-term stability of cardiovascular implants [58]. Conventional metals are generally not compatible with tissues. This poor biocompatibility can cause acute thrombosis and long-term restenosis. As a result, the metallic stent can fail due to the response of the vascular smooth muscle cells (VSMCs) or decreased function of the endothelial cells in the vessel [59]. A frequently used approach to improve the biocompatibility of the vascular stent is to coat the traditional metallic surface with materials such as hyaluronan [60], tantalum [61], expanded polytetrafluoroethylene [62], or silicon carbide [63]. These surface modifications all help improve the biocompatibility of the stent with the VSMCs and decrease the interactions of the vascular stent with blood cells. Other options have been suggested to alter the original surface of the metallic vascular stents to enable them to interact with cells [64]. The modification of physical structure may be beneficial in the long-term to design of artificial implants.

The biocompatibility of stents requires design optimisation. The biocompatible material gold is thought to be ideal for coating coronary stents because of its radio-opaque properties [65]. Some studies evaluating the biocompatibility of gold-coated stents suggest that they are equivalent to uncoated steel stents [66]. However, other studies, albeit with patients enrolled who were at higher risk for restenosis, concluded that these stents may increase neointimal hyperplasia compared to uncoated stents [67]. Silicon carbide is an inert semiconductor that can also be coated onto prosthetic surfaces and has been known to be relatively biocompatible and hemocompatible in in vitro studies [52]. Stents coated with silicon carbide also appear to be less thrombogenic than bare metal stents when implanted in human coronary arteries [68]. Overall, observational studies examining gold-coated stents show conflicting results, and the restenosis rates are no better than those obtained with uncoated steel stents [69].

In addition to biocompatibility, cellular function is another important concern in the design of artificial implants [70]. Biocompatibility does not guarantee optimal cell function. In many situations, biocompatibility must be balanced with cell function, such as when stimulation of VSMC proliferation causes restenosis in cardiovascular stents. Restenosis results from the proliferation of smooth muscle cells in the vessel wall in response to acute vessel wall injury induced by angioplasty. Recurrent stenosis and late-stage thrombosis remain significant limitations to successful stent function after stenting peripheral or coronary atherosclerotic lesions [71]. A nanotopographical platform with continuously varied structure could help achieve an implant surface topography that balances biocompatibility and function.

1.4.2 Design of dental implant for osseointegration

For dental implants, surfaces are moderately roughened to promote osseointegration [51, 72]. Studies have shown that osteoblast-like cells favor microstructured surfaces [73-76]. Roughened surfaces enhance the focal adhesion and guide cytoskeletal assembly and membrane receptor organization [18, 77]. Moreover, rough implant surfaces have been shown in *in vitro* experiments to enhance the adsorption of fibronectin and albumin [78-79], which are important extracellular matrix molecules for cell focal adhesion. Methods including acid-etching, plasma-spraying, grit-blasting, vapor deposition, anodization, and other coating technologies have been developed to fabricate micro- and nanostructures. These different modifications, which result in a variety of surface chemistries and topographies, have led to ambiguous responses by osteoblasts [80-81].There are considerable disagreements concerning the optimal physicochemical properties and surface geometries for the endosseous portion of a dental implant.

Identifying the optimal surface for the bio-implant interface is an important task in tissue engineering [82-83]. Nanoscale modification of the implant surface may alter the surface reactivity of endosseous implants. The surface roughness influences the production of growth factors, cytokines and mRNAs, suggesting that the substrate modulates the activity of the cells that are adjacent to an implant; this roughness subsequently affects the adjacent skeletal tissue response and implant success [84-85]. Moreover, surface topography affects the amount of bone that is deposited adjacent to the implants and bone, and its formation can be guided by the specific implant topography [86]. Thus, surface topography plays a critical role in the interaction of dental implants with the adjacent tissues [87-88]. Nanoscale topography may provide biomimetic surfaces that support hydroxyapatite mineral formation [89] and the related organic phase guidance of bone mineralization [90].

1.5 Survey and control of cell behaviors by nanotopography

The development of invasive and metastatic properties in cancer cells is complicated [91-94]. Invasion of cancer cells begins when cells break away from the primary tumor and penetrate the surrounding tissue, followed by movement into the circulatory system, transportation through the body, and the establishment of a secondary tumor. Changes in motility and the production of enzymes that break through surrounding tissue are characteristic of invasive cancer cells. A fast and convenient platform for cancer diagnosis should be beneficial in obtaining additional factors and parameters that control or manipulate the invasive properties of cancer cells. Thus, utilization of assemblies containing a range of nanostructures should be capable of distinguishing among cancer cell lines of various stages and also provide optical parameters that are useful in the design and evaluation of artificial implants for tissue engineering.

Here we proposed to study cellular responds to nanotopography with different feature sizes and to analyze the differences in physical expressions of cells. The highly packed and uniformly distributed nanodot arrays with defined diameter and depth were fabricated by using aluminum nanopores as a template during oxidation of tantalum thin film [95]. The controllable pore size of aluminum oxide served as a convenient mold to fabricate tantalum into nanodot array of defined diameter. The 2D structure containing nanodots of uniform size have served as a defined nanolandscape to investigate cellular response to topological variation. We fabricated arrays of nanodot surfaces containing dot diameters ranging between 10 and 200 nm. This study is based on the hypothesis that nanotopography may modulate and control the growth, proliferation, and biological function of cells. We determined the nanostructure that achieved maximum cell growth and adhesion. Functional performance, indicated by the expression of representative genes, indicated that the optimized range of nanostructures derived balanced high biocompatibility and cell function.

An integrated nanodevice containing nanodot arrays with dot diameters ranging from 10 nm to 200 nm can be used to evaluate cell behavior. Nanodevices may be used as a detecting platform for the rapid modulation of proliferation, apoptosis, invasive ability, and cytoskeletal reorganization in different cell types. The topologic design of implant surfaces is one of the important factors for the fabrication of medical implants [11, 96]. We can use this platform to survey the optical parameters for various cells *in vitro*. This strategy will serve as a convenient and fast tool for tissue engineering and cancer diagnosis.

2. Materials and methods

2.1 Fabrication of nanodot arrays

Nanodot arrays were fabricated as described previously [95]. A TaN thin film of 150 nm thickness was sputtered onto a 6-inch silicon wafer, followed by the deposition of 3 μm-thick aluminum onto the top of the TaN layer. Anodization was carried out in 1.8 M sulfuric acid at 5 Volts for the 10 nm nanodot array, or in 0.3 M oxalic acid at 25 Volts, 60 Volts, and 100 Volts for the 50 nm, 100 nm, and 200 nm nanodot arrays, respectively. Porous anodic alumina was formed during the anodic oxidation. The underlying TaN layer was oxidized into tantalum oxide nanodots using the alumina nanopores as template. The porous alumina was removed by immersion in 5 % (w/v) H_3PO_4 overnight. A thin layer of platinum (~5 nm) was sputtered onto the structure to improve biocompatibility. The dimension and homogeneity of the nanodot arrays were measured and calculated from images taken by JEOL JSM-6500 TFE-SEM and by atomic force microscopy (AFM). The fabricated nanodot arrays were cut into 1 cm x 1 cm squares and integrated into a 3 x 3 matrix that was set in a PDMS frame. The PDMS frame was molded in a glass template fabricated by photolithography [97]. Before curing, the template-covered PDMS was held for one hour to allow all bubbles in the PDMS layer to escape. The curing process was performed by heating the PDMS to 75^{o}C in an oven for approximately 45 minutes. The final matrix contained a flat-surfaced square at the center surrounded by nanodot arrays ranging from 10 nm to 200 nm.

2.2 Cell cultures

Characteristics of the cell lines are summarized in Table 5 HELA, PA-1, and MG63 cells were cultured in Dulbecco’s Modified Eagle’s Medium (DMEM) supplemented with 10% fetal bovine serum (FBS) and incubated in 5% CO2 at 37℃. ES2 cells were cultured in DMEM supplemented with 10% fetal calf serum (FCS) and incubated in 5% CO2 at 37℃. C33A cells were cultured in MEM Alpha supplemented with 10% FBS and incubated in 5% CO2 at 37℃. TOV-112D and TOV-21G cells were cultured in MCDB105 and Medium199 supplemented with 15% FBS and incubated in 5% CO2 at 37℃. H9c2 rat cardiomyoblasts were purchased from BCRC (Bioresource Collection and Research Center, Hsinchu, Taiwan) and cultured on various nanodot arrays with Dulbecco's Modified Eagle's Medium (DMEM) containing 10% fetal bovine serum (FBS, Gibco) and supplemented with 4mM L-glutamine at 37 ℃ in a humidified 5% CO2 incubator.

2.3 Measurement of cell attachment by cell density

Cells were double stained using 4',6-diamidino-2-phenylindole DAPI and phalloidin. Cells were harvested and fixed using 4% paraformaldehyde diluted in PBS for 30 min, followed by 3 washes in PBS. Cell membranes were permeabilised during 10 min incubation in 0.1 % Triton X-100, followed by 3 PBS washes. Cells were incubated with phalloidin and nuclei counterstained with DAPI for 15 min at room temperature. Samples were mounted and imaged using a Leica TCS SP2 confocal microscope. Cell number was counted using ImageJ software and expressed in terms of cell density.

2.4 Scanning electron microscopy (SEM)

Harvested cells were fixed using 1% glutaraldehyde in PBS at 4℃ for 20 min, followed by post-fixation in 1% osmium tetraoxide for 30 min. Ethanol dehydration was performed using a series of 10 min incubations in 50, 60, 70, 80, 90, 95, and 100% ethanol and air dried. The specimen was sputter-coated with platinum and examined by JEOL JSM-6500 TFE-SEM at an accelerating voltage of 5 keV.

2.5 Immunostaining

Cells were harvested and fixed using 4% paraformaldehyde in PBS for 15 min followed by 3 PBS washes. Cell membranes were permeabilised using 0.1% Triton X-100 incubation for 10 min, followed by 3 washes in PBS. The membranes were then blocked using 1% BSA in PBS for 1 hr and washed again in PBS 3 times. The sample was incubated with anti-vinculin antibody (diluted in 1% BSA solution) and phalloidin for 1 hr, followed by incubation with Alexa Fluor 488 goat anti-mouse antibody for 1 hr and then 3 washes in PBS. Samples were mounted and imaged using a Leica TCS SP2 confocal microscope.

2.6 Bromodeoxyuridine (BrdU) proliferation assay

Cells were incubated with BrdU drug for 6 hours prior to harvest. Cells were then harvested and fixed using 4% paraformaldehyde in PBS for 15 min followed by 3 PBS washes. Cell membranes were permeabilised using 10 min incubation in 0.1% Triton X-100, followed by 3 PBS washes. A 2N HCl solution was applied to break the nuclear membranes. Next, cells were blocked using 1% BSA in PBS for 1 hr. Cells were incubated with anti-BrdU antibody (diluted in 1% BSA) for 24 hours at 4℃, followed by incubation with Alexa Fluor 488 goat anti-mouse antibody and DAPI for 1 hr and then 3 washes in PBS. Cells were then counterstained using BrdU and DAPI to image the nucleus. Samples were mounted and imaged using a Leica TCS SP2 confocal microscope. ImageJ software was used to determine BrdU-labelled cell numbers.

2.7 Caspase-3 activity assay

The EnzChek Caspase-3 Assay Kit #2 (Invitrogen, USA) was applied to evaluate the caspase-3 activity, using the procedures provided by the manufacturer. Cells were harvested and counted, followed by incubation with the lysis buffer for 30 minutes. The cell lysate was centrifuged, and the supernatant was transferred to microplate wells containing Z-DEVD–R110-substrate-working solution followed by a 30 minute incubation at room temperature. The fluorescence was measured using an ELISA microplate reader (Perkin Elmer, USA) with an excitation wavelength at 496 nm and an emission wavelength at 520 nm. The caspase-3 activity was normalized to cell counts.

2.8 Quantitative real-time PCR

Oligo primers used to amplify genes of interest were designed based on the sequences provided in previous reports (Table 1) [98-100]. The specificity of synthesised primers was verified by polymerase chain reaction (PCR) using reverse-transcribed mRNA extracted from cells as a template. The sizes of PCR products were resolved using agarose gel electrophoresis.

Table 1 *Primer sequences*

Gene	**Forward sequence**	**Reverse sequence**
GAPDH	gcctacctcatgggactgaa	acattctgccctttggtgac
Hsp27	gagtggtctcagtggttcag	ccttccttggtcttaactgtg
Hsp60	acaagtgatgttgaagtgaatg	atgcaggaattttaagtgctc

Hsp70	cctacttcaacgactcgcag	cttcctcttgaactcctccac
Hsp90	gtcttctctcgcttctcactt	vtatctgtgggaggggattct
beta-MHC	gcctacctcatgggactgaa	acattctgccctttggtgac
GATA-4	agaaggcagagagtgtgtca	cagtgtggtggtggtagtct
PAI-1	gaacgccctctattgtgccgaac	ctctgttggattgtgccgaac
ANF	tgggctccttctccatcacc	gccaaaaggccaggactgac
RAMP2	ttactgctgctgttgctgct	aggaaagggatgaggcagat
RAMP3	acctggtcgtgtcaaagtcc	ccacaccttccagatgacct
Bcl-2	gctacgagtgggatactgg	gtgtgcagatgccggttca
Bax	ctgcagaggatgattgctga	gatcagctcgggcactttag

Total RNA was extracted from 1.8×10^5 cells using TRI-reagent (Talron Biotech) according to the manufacturer's specifications. The RNA was isolated using chloroform extraction and isopropanol precipitation. The RNA extract was immediately purified using an RNeasy Mini Kit (Qiagen) to remove impurities and unwanted organic compounds. Purified RNA was resuspended in DEPC-treated water and quantified by OD$_{260}$. The OD$_{260}$-to-OD$_{280}$ ratio usually exceeded 2.0 at this stage. For cDNA synthesis, 1 μg total RNA was annealed using 1 μg oligo-dT primer, followed by reverse transcription using SuperScript® III Reverse Transcriptase (Invitrogen) in a total volume of 50 μl. Between 0.2 and 0.5 μl of the reverse transcription reactions were used for quantitative qPCR using SYBR Green I performed on an iCycler iQ5 (Bio-Rad Laboratories). The cycling conditions were as follows: 1 cycle of 5 min at 95℃ and 50 cycles of 20 s at 95℃, 20 s at 55℃, and 40 s at 72℃. Fluorescence was measured after each 72℃ step. Expression levels were obtained using threshold cycles (Ct) that were determined by the iCycler iQ Detection

System software. Relative transcript quantities were calculated using the ΔΔCt method. The gene GAPDH was used as a reference gene and was amplified along with the target genes from the same cDNA samples. The difference in threshold cycles of the sample mRNA relative to GAPDH mRNA was defined as the ΔCt. The difference between the ΔCt of the control cells and the ΔCt of the cells grown on nanodot arrays was defined as the ΔΔCt. The fold change in mRNA expression was expressed as $2^{\Delta\Delta Ct}$. The results were expressed as the mean ± SD of six experiments.

2.9 Western blot

Cultured cells were lysed and centrifuged at 12000*g* for 2 min at 4℃. The supernatants were transferred to new Eppendorf tubes and protein concentrations were defined using UV/VIS spectroscopy. After the protein concentrations were defined, solutions were mixed with 4X sample buffer and lysis buffer to a final concentration of 1 μg/μL protein. Samples were heated at 95°C for 3 min and cooled at 0℃ for 3 min; this step was repeated twice. Proteins were separated using 10% SDS-PAGE gels and transferred to PVDF membranes. Nonspecific protein binding was blocked using a 5% milk solution at 4℃ overnight. The membranes were subsequently blotted at 4℃ overnight using the specific antibodies indicated for each experiment, which were diluted in blocking buffer. Specific primary antibodies were blotted using second antibodies in the blocking buffer at room temperature for 1 hr. Chemiluminescent detection was performed using western blotting luminol reagent and oxidising reagent (U.S.A.).

2.10 Dental implant

The following implant surfaces were investigated: a titanium substrate with a calcium phosphate (CaP) treatment (Implant A), a titanium substrate with CaP plasma-sprayed coating (Implant B), a titanium surface having a titanium plasma-sprayed coating (Implant C), and an uncoated titanium substrate with a machined surface (Implant D). Four types of commercially available dental implants were employed in the clinical tests. Electron microscopy was performed to examine the microstructures and nanostructures of the implants.

2.11 von Kossa staining

MG63 cells were harvested and fixed with 95 % ethanol for 1 hour and then washed three times with DI water. The samples were treated with a 5 % silver nitrate solution, exposed to UV light for 20 minutes, and then washed three times with DI water. The samples were treated with a 5 % thiosulphate solution for 5 minutes and then washed three times with DI-water [101-102]. We randomly picked 50 cells for each condition and calculated the area of the nodule per cell relative to the area of the nodule per cell cultured on a flat surface.

2.12 Alizarin Red S staining

The MG63 cells on the substrates were washed with PBS and fixed with 4 % paraformaldehyde for 10 min. The fixed cells were soaked in 0.5 % Alizarin Red in PBS for 10 minutes at room temperature and then washed with water to remove the remaining stain [103-104]. After staining, the specimens were visualized with an objective microscope. We randomly picked 50 cells for each condition and calculated the area of the stain per cell relative to the area of the stain per cell cultured on a flat surface.

2.13 Statistics

The means and standard deviations were calculated for the recorded data.

Student’s t-test was employed to determine data sets that differed significantly from one another, and significance was defined as a p-value < 0.05.

3. Results and discussion

3.1 Fabrication of nanodot arrays

Nanodot arrays were fabricated, as described previously, by AAO processing on tantalum-coated wafers. Tantalum oxide nanodot arrays with dot diameters of 10 nm, 50 nm, 100 nm, and 200 nm were constructed on the silicon wafers. To provide a biocompatible and unique interacting surface, ~5 nm-thick platinum was sputter-coated onto the top of the nanodots. Scanning electron microscopy (SEM) and AFM images showed diameters of 15±2.8 nm, 58.1±5.6 nm, 95.4±9.2 nm, and 211.5±30.6 nm for the 10 nm, 50 nm, 100 nm, and 200 nm dot arrays, respectively (Figure 1). The average heights were 11.3±2.5, 51.3±5.5, 101.1±10.3, and 154.2±27.8 nm, respectively. Dot-to-dot distances were 22.8±4.6 nm, 61.3±6.4 nm, 108.1±2.3 nm, and 194.2±15.1 nm, respectively. The dimensions of the nanodots were well-controlled and highly defined.

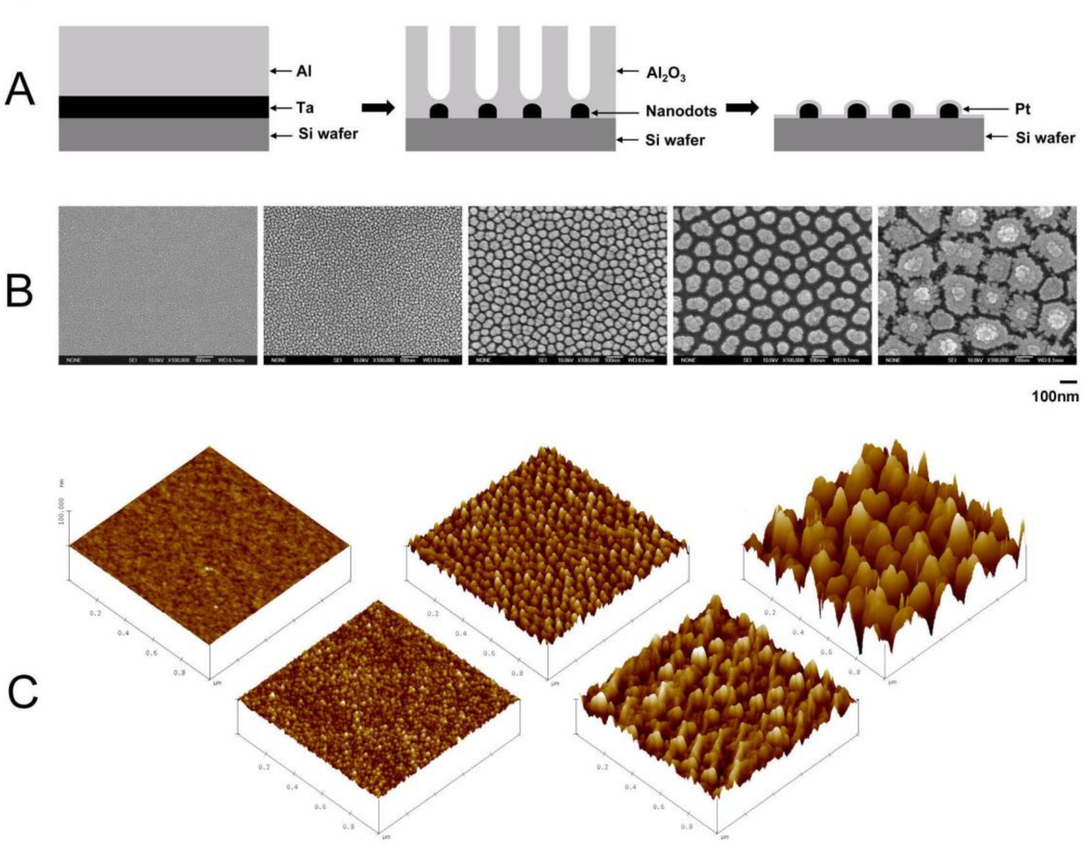

Figure 1 *Fabrication of tantalum-based nanodot arrays using AAO processing. (A) Schematic representation of fabrication procedure. (B) SEM images of the fabricated nanodot arrays. (C) AFM images of the fabricated nanodot arrays. Images are arranged from left to right: unprocessed silicon (Si), 10 nm nanodot array (10 nm), 50 nm nanodot array (50 nm), 100 nm nanodot array (100 nm), and 200 nm nanodot array (200 nm).*

3.2 Nanodot array modulates cell adhesion and induces an apoptosis-like abnormality in 3T3 fibroblast

3.2.1Cell response to nanodot arrays

NIH-3T3 cells were cultured on fabricated nanodot arrays and on flat wafers at a density of 1,000 to 5,000 cells per square centimeter. Cells were harvested at 24 hr (day 1), 48 hr (day 2), 72 hr (day 3), and 96 hr (day 4) after seeding. SEM was performed to examine the morphology of the cells (Figure 2). The side-view of the

SEM images provided alternative angles for evaluating the morphological change of cultured cells. Cells grown on the control surface and the 10 nm nanodot array remained flat and extended throughout the course of incubation. Cells grown on the 50 nm nanodot array began to show an abnormal appearance on day 4. The abnormal cells underwent a transformation of the main cell body into sub-cellular spheres of ~5 microns in diameter. On day 4, spherical sub-cellular cell bodies were visible. For cells grown on the 100 nm nanodot array, a comparable morphology occurred as early as day 3, while for the 200 nm nanodot array, the morphological aberration started from day 2. The proportion of cells undergoing this morphological change was higher, and the event was triggered earlier, on the 100- and 200 nm nanodot arrays (figure 3A).

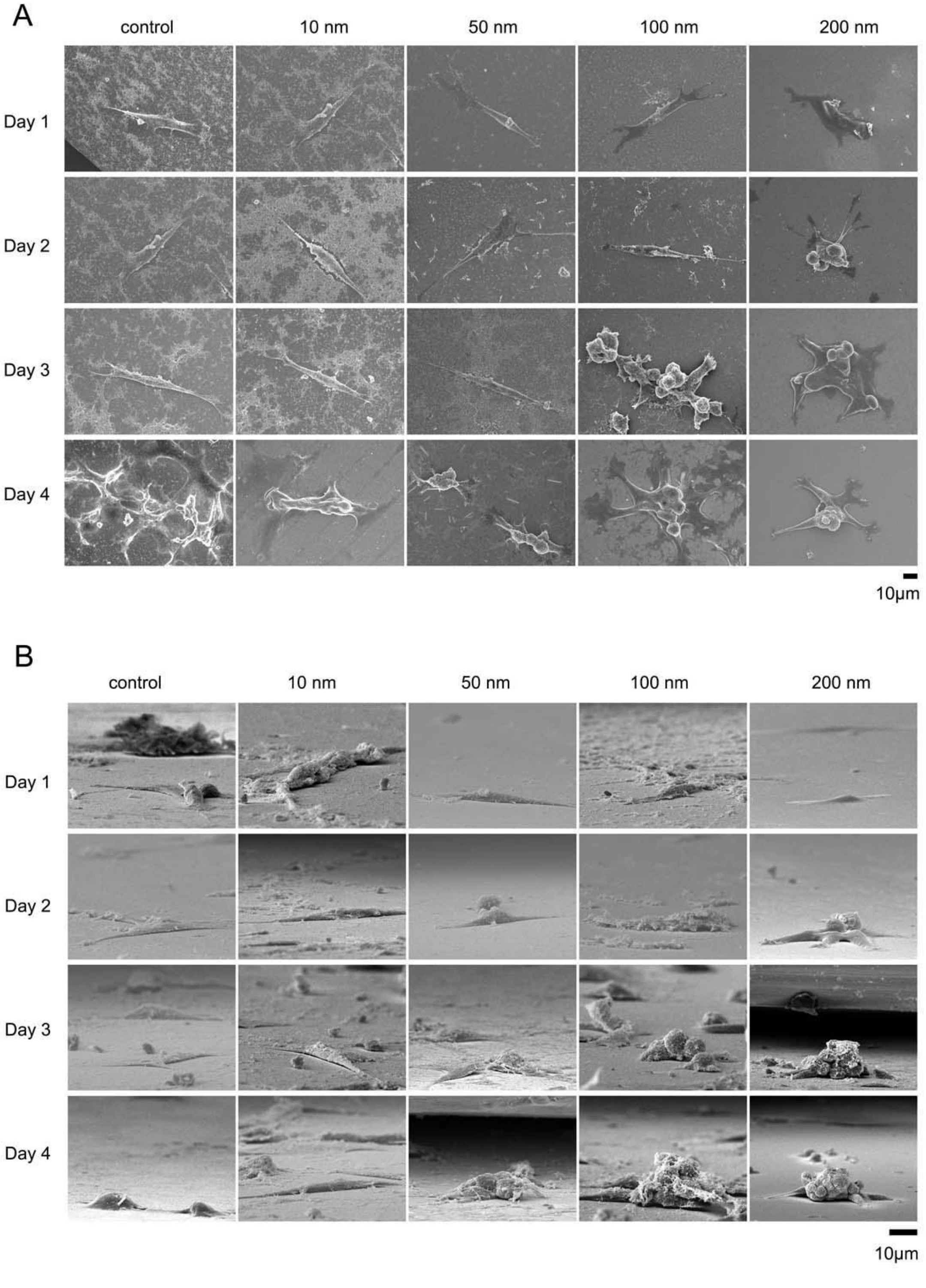

Figure 2 *SEM images of cells seeded on the nanodot arrays. NIH-3T3 cells were seeded on a flat silicon surface, 10 nm nanodot array (10 nm), 50 nm nanodot array (50 nm), 100 nm nanodot array (100 nm), and 200 nm nanodot array (200 nm). The cells were harvested at 24 hr (Day 1), 48 hr (Day 2), 72 hr (Day 3), and 96 hr (Day 4) after seeding. SEM images were taken. Representative images are shown: (A) top view,*

(B) side view.

3.2.2Nanotextured surface triggers apoptosis-like events of fibroblasts

The morphology of the abnormal cells resembled cells proceeding in programmed cell death. Caspase activity is the hallmark for apoptosis. Thus, the occurrence of apoptosis-like events was verified by a caspase-3 activity assay performed on cells seeded on nanodot arrays following the time course (figure 3B). The onset, time-dependent accumulation, and size-dependent profile of caspase-3 activity matched the proportion of cells undergoing morphological transformation on the nanodot arrays. The nanotopography triggered apoptosis-like events for cultured cells in a size-dependent and time-dependent manner.

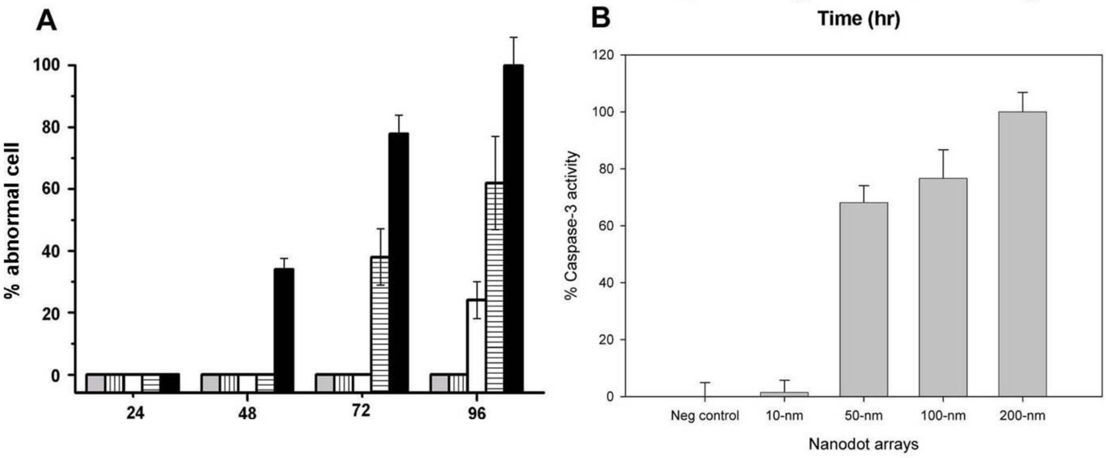

Figure 3 *Apoptosis occurred in cells cultured on nanodot arrays. (A) The percentage of cells with abnormal morphology calculated from SEM images. Bars depict percent apoptotic cells grown on the flat silicon surface (grey), 10 nm nanodot array (vertical line), 50 nm nanodot array (empty), 100 nm nanodot array (horizontal line), and 200 nm nanodot array (filled). (B) Caspase-3 activity for cells cultured 96 hrs on the nanodot arrays. Values were averaged from 6 sets of independent experiments and were expressed as mean value ± standard deviation.*

Cells grown on the nano-scaled structure could engulf any loose nanoparticles. The endocytosis of the remnants might induce the observed abnormalities. To exclude the possibility that the abnormality was due not to the growth on the nano-structure but to the endocytosis of nanodots, the used arrays were thoroughly cleaned and examined under an electron microscope. The SEM images indicated that the nanodot structures of the used 100 nm and 200 nm nanodot arrays were intact even after a prolonged culturing of cells (Figure 4).

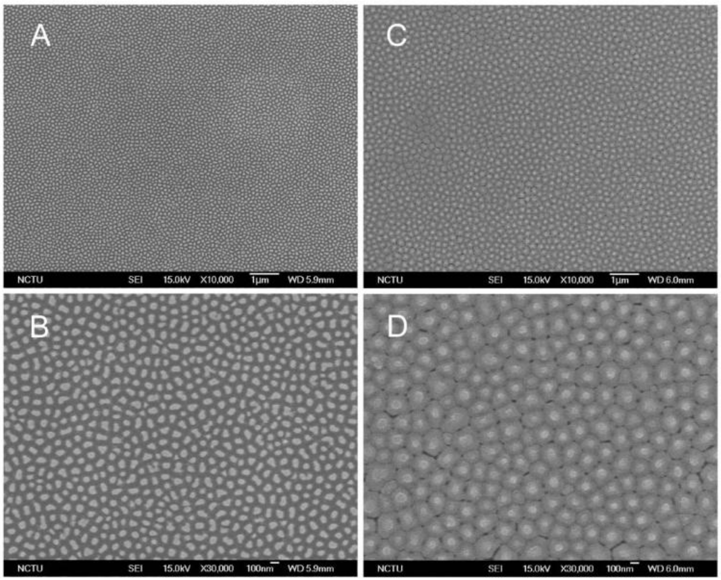

Figure 4 *SEM images of the used nanodot arrays. Nanodot arrays of 100 nm and 200 nm were cleaned and washed thoroughly after culturing cells. SEM images were taken on the cleaned nanodot arrays of (A, B) 100 nm and (C, D) 200 nm.*

3.2.3Cell adhesion and reorganization of the cytoskeleton were required for the nanotopography-induced cellular abnormality

The formation of focal adhesions, reflected by the attachment of filopodia to the substratum, indicates normal growth for cultured cells [57]. The number of filopodia extended from the cells decreased for cells grown on nanodot arrays larger than 50 nm (Figure 5). For cells seeded on the 200 nm nanodot array, very few filopodia were found. Cells grown on larger-sized nanodot arrays lost the ability to establish filopodia attachment. Further examination indicated that cellular attachment was defective for cells grown on the 100 nm nanodot array (Figure 6).

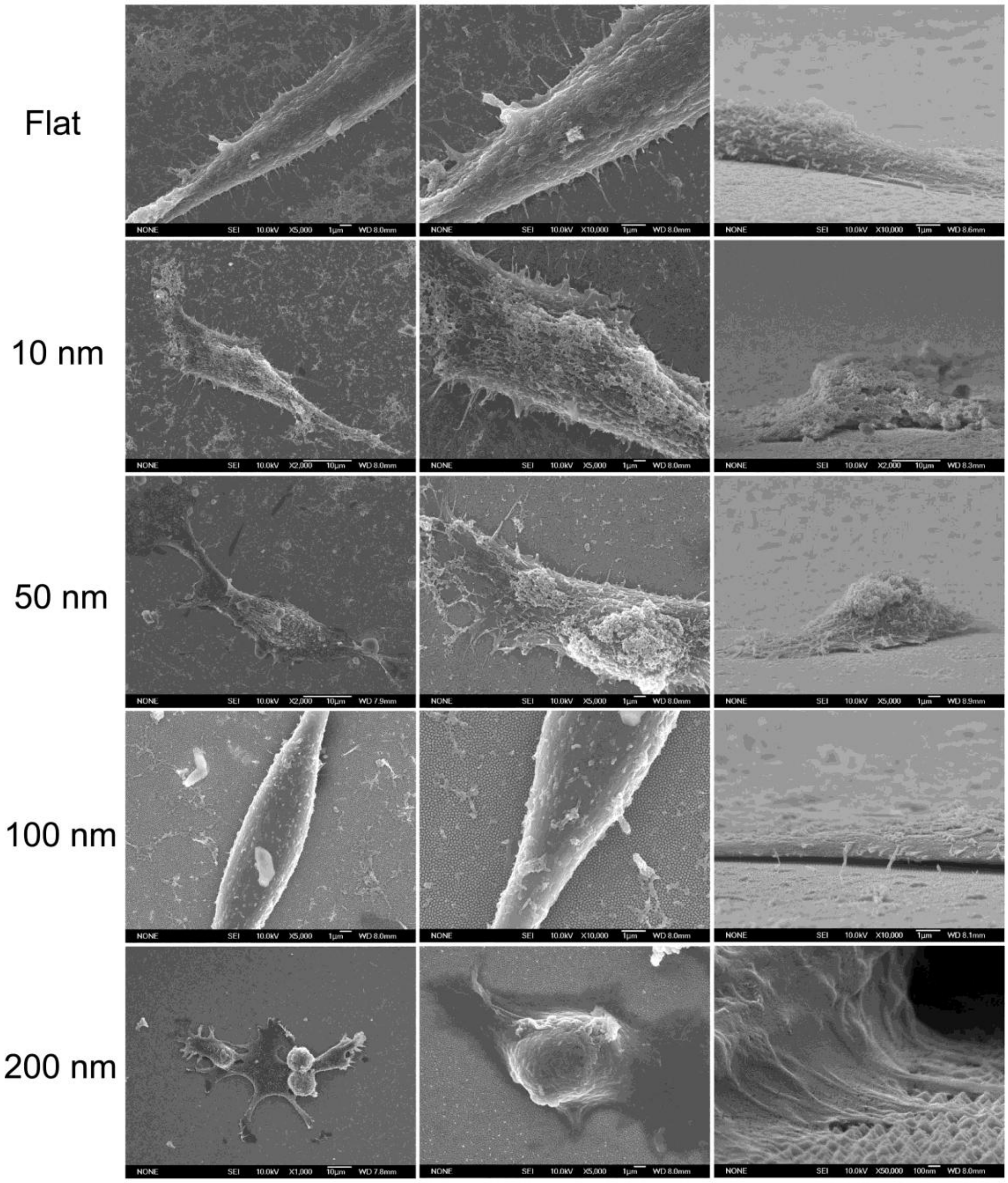

Figure 5 *SEM images of NIH-3T3 cells cultured on nanodot arrays to show the filopodia extended from cells. Typical the cells were shown to elicit the detail of cellular structure.*

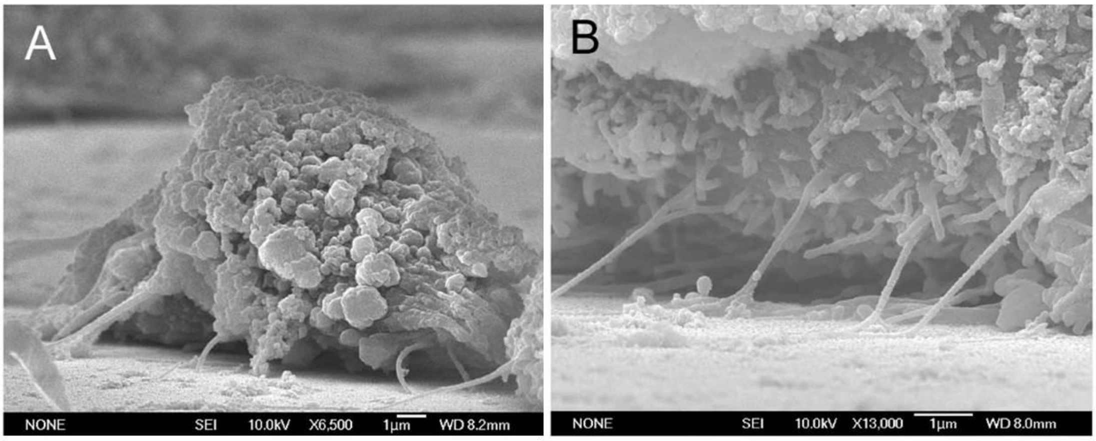

Figure 6 *SEM side-view images showing the poor cell attachment of NIH-3T3 cells grown on the 100 nm nanodot array.*

Topology and surface chemistry might share a common pathway for directing cell behavior. Focal adhesions are mediated by cell adhesion through receptor-ligand binding [105-106]. The inability of cells to establish filopodia attachment on a nanolandscape might be prevented by a surface modification with ligands. We coated the 100 nm nanodot array with BSA, FN, or type I collagen. Pre-treatment with BSA did not prevent the nanotopography-induced apoptosis-like abnormality, while FN and collagen I coating completely averted cellular abnormality (Figure 7). FN and collagen are native substrates of integrins, the key transmembrane proteins of focal adhesions. The prevention of programmed cell death by FN- or type I collagen-enforced cell anchorage indicates that the topography-induced apoptosis-like abnormality could be overridden by receptor-mediated cell adhesion.

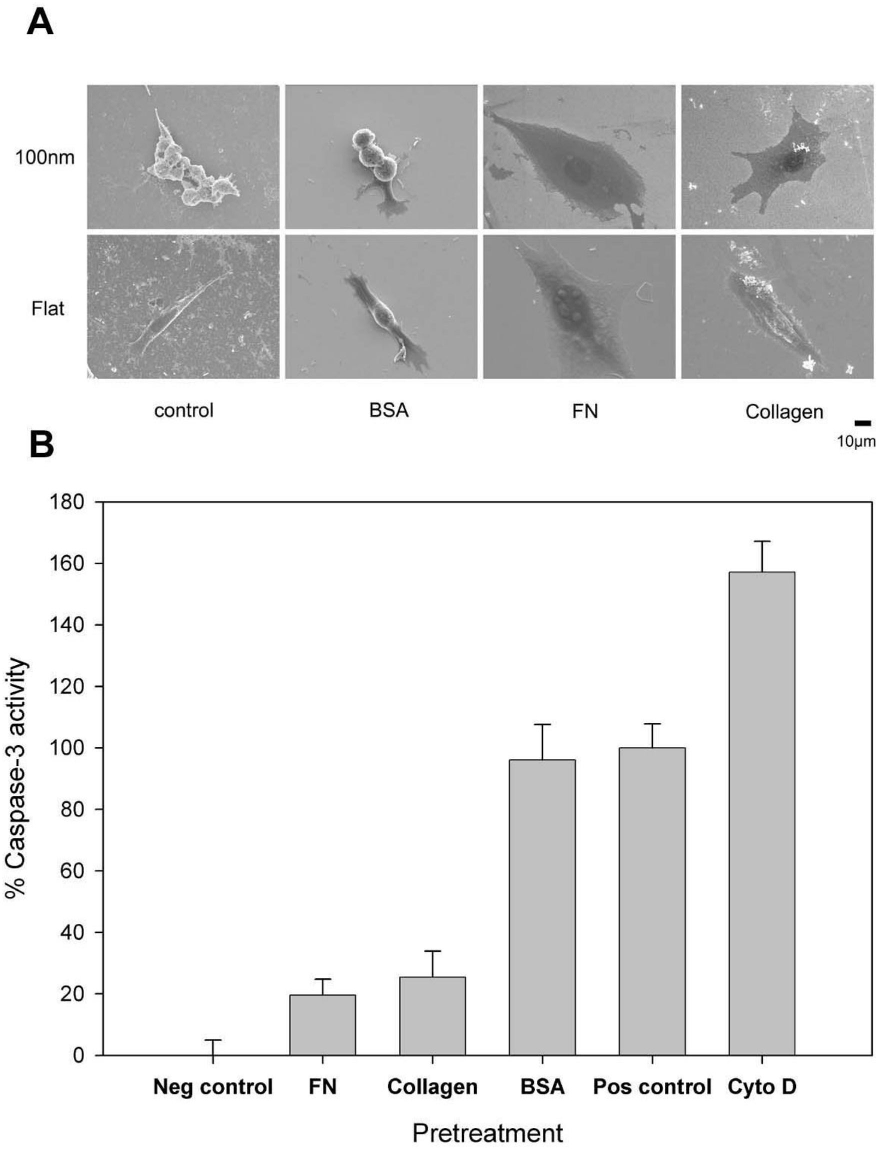

Figure 7 *Effects of BSA-, FN-, and type I collagen-coating on the nanotopography-induced apoptosis-like abnormality. Cells were seeded on 100 nm nanodot arrays and flat wafers pretreated with BSA-, FN-, and type I collagen. Cells were harvested on day 4. SEM was performed to visualize the morphology of the cells (A). Apoptosis-like events occurred were quantified by the caspase-3 activity assay (B).*

To evaluate the role of adhesion molecules in the nanotopography-induced apoptosis-like events, immuno-staining specific to actin filaments and vinculin was performed on cells grown on the nanodot arrays (Figure 8). Well-organized actin filaments were visible for cells grown on the flat wafer and on the 10 nm nanodot array. This tight arrangement was gradually lost in cells grown on the 50 nm array and completely disappeared on the 100 nm and 200 nm arrays. Vinculin staining indicated formation of focal adhesions. Vinculin was detected and well-distributed for cells grown on the flat surface and on the 10 nm array. The amount of vinculin staining decreased for the 50 nm array and almost disappeared for the 100 nm and 200 nm arrays. This immunostaining indicated that the nanotopography retarded or inhibited the assembling of focal adhesions.

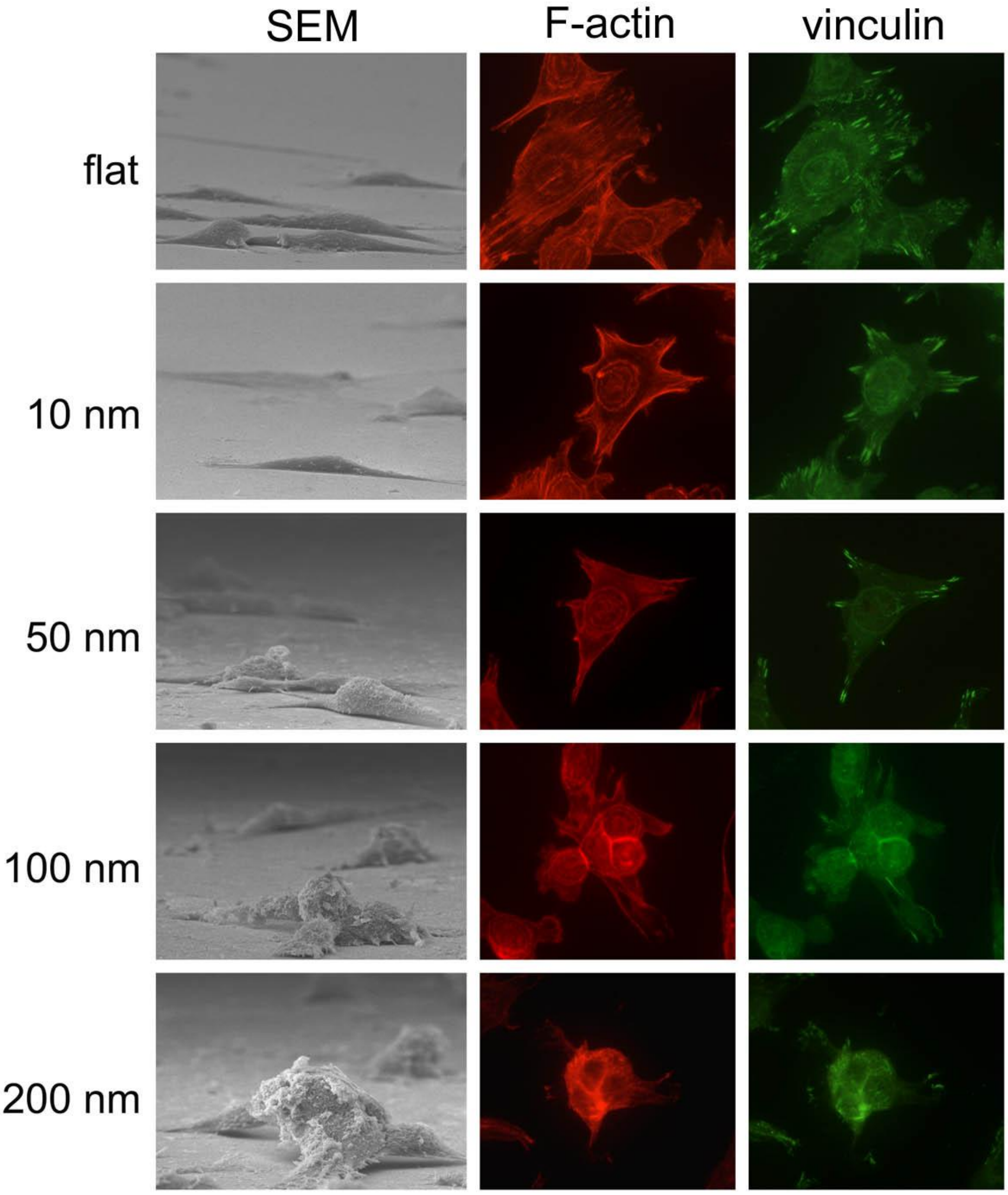

Figure 8 *Immunostaining to show organization of actin filament and distribution of vinculin in cells cultured on 10 nm, 50 nm, 100 nm, and 200 nm nanodot arrays and on flat surfaces. Cells were seeded on the arrays for 96 hours before harvest. The sample*

was incubated with anti-vinculin antibody (properly diluted in 0.5 % BSA) and phalloidin, followed by incubating with Alexa Fluor 488 goat anti-mouse antibody.

Micro-topography has been shown to be advantageous to cell growth. Three-dimensional fibrous structures provide an in vivo-like environment that enhances the growth of cells. Micro-scaled grooves and valleys direct the growth of cells. In the current study, the nanotopography of the nanodot arrays generated an apoptotic signal leading to the suicide of cells. Since a micro-topography of 100 nm nanofibers promotes cell proliferation and adhesion, the apoptosis induced by the nanotopography is unexpected. For cells cultured on 13 nm deep nano-islands, increased cell adhesion, proliferation, cytoskeleton, and extracellular matrix remodeling were observed [107-108]. A reduced cell adhesion and cytoskeletal organization was shown for cells cultured on 95 nm deep nano-islands. Although the exact shape and topology is different for the nanodot arrays applied in the current study, the results from both studies shared a common theme that a dot-like nanotopology with dimensions at about 100 nm reduced cytoskeletal organization. Although cellular abnormality was not stated, the result from the nanoisland study is consistent with the current study.

3.3 *Topographic control of the growth and function of cardiomyoblast H9c2 cells using nanodot array*

3.3.1 *Cell attachment and proliferation of cardiomyoblasts grown on arrays of nanodots*

To evaluate the attachment level of cardiomyoblasts to various nanodot arrays, H9c2 cardiomyoblasts were cultured on fabricated nanodot arrays or on flat wafers at densities between 2,000 and 5,000 cells per square centimetre. Cells were harvested 24 hr (day 1), 72 hr (day 3), and 120 hr (day 5) after seeding. DAPI staining was performed to identify viable cells. Immunostaining using anti-actin filament IgG was performed to verify the normal growth state of cells stained by DAPI. The density of viable cells was obtained by counting DAPI-stained cells (Figure 9). On day 1, most cells cultured on the 10-, 50-, or 100 nm nanodot arrays grew well, and the densities of cells cultured on arrays were comparable that on flat controls. In contrast, at day 1, cells cultured on the 200 nm nanodot arrays exhibited a 64.9% reduction in cell number compared to a flat surface. On day 3, an increase in cell viability was generally observed for cells cultured on flat, 10 nm, and 50 nm nanodot surfaces; however, there is a 53.7% and 72.6% reduction, respectively, in cell densities observed on the 100- and 200 nm nanodot arrays. The reduction in cell number observed on day 5 for flat surfaces and 10 nm nanodot arrays is apparently due to the overgrowth of cells, which occupied more than 90% of the culture dish surface area rather than to the nanotopology of the surface. On day 5, cells cultured on the 100- or 200 nm nanodot arrays exhibit a small increase in the viability of cells compared to day 3 and day 1, but a significant retardation of growth when compared to flat surfaces.

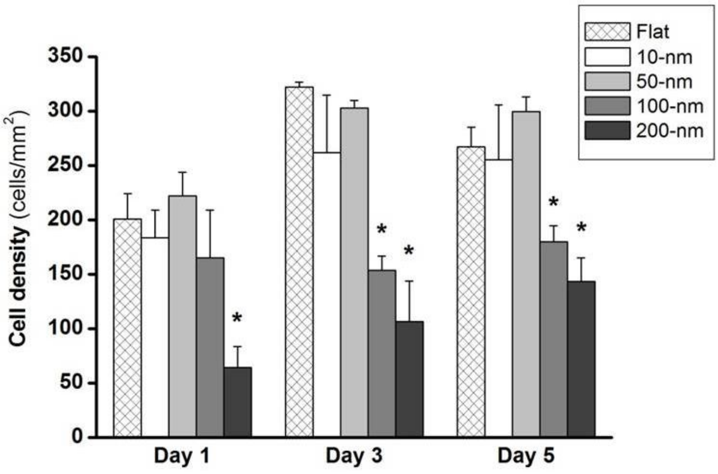

Figure 9 *Time course experiments to determine the dependence on nanotopography of*

*cell density of H9c2 cardiomyoblasts. Cardiomyoblasts seeded on nanodot arrays of various sizes were harvested after 1, 3, or 5 days culture. Bar chart of cell density versus different sizes of nanodots. Cells were double-stained using DAPI and phalloidin. Cell density was calculated based on cell number counts. The mean ± SD from at least 3 experiments is shown. *p<0.05 when compared with flat control surfaces.*

Bromodeoxyuridine (BrdU) cell proliferation assay is a non-isotopic immunoassay for quantification of newly synthesised DNA in actively proliferating cells. BrdU was applied to differentiate the newly proliferated cells from pre-existing culture. Additionally, DAPI was used to stain the nuclei, an indicator of the total number of viable cells (Figure 10). On day 1, maximum proliferation was observed in cells grown on 50 nm nanodot arrays, which was approximately 2-fold greater than cells grown on flat surfaces. On day 3, significant proliferation is still observed; the reduction in growth rate is likely due to the saturation of cells.

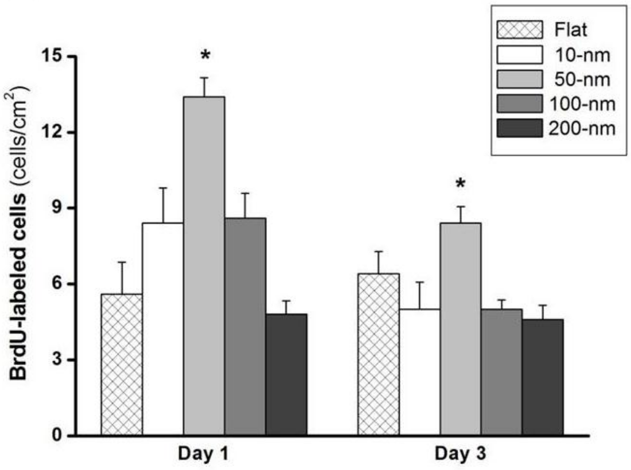

Figure 10 *Time course experiments to determine the dependence on nanotopography of cell proliferation of H9c2 cardiomyoblasts. Cardiomyoblasts seeded on nanodot arrays of various sizes were harvested after 1 and 3 days culture. Bar chart of proliferation versus dot size. Cells were incubated with BrdU and stained with a mouse anti-BrdU monoclonal antibody for 6 hours and subsequently examined under a fluorescence microscope. Newly proliferated cells were also counted. The mean ± SD from at least 3 experiments is shown. *p<0.05 when compared with flat control*

surfaces.

In summary, optimal growth occurred on 50 nm nanodot arrays. These permitted maximum cell attachment even when the cell density reached saturation. On flat surfaces and 10 nm nanodots, cardiomyoblasts grew well; however, a minor decrease in cell density was observed on day 5 when cells were grown to saturation. Nanodots of 100- and 200 nm prevented viable growth of cardiomyoblasts, as indicated by 53.7% and 72.6% reductions, respectively, on day 3. Maximum proliferation occurred in cells grown on 50 nm nanodots, which was approximately 2-fold more than cells grown on flat surfaces.

3.3.2Nanotopography-modulated morphology of cardiomyoblasts

Morphology is an important index for cell growth. Flat and extended cells indicate healthy and proliferate growth. Nanotopography is known to modulate cell morphology of NIH-3T3 cells. Biochemical and genetic evidence indicated that apoptosis occurs in cells with abnormal morphology.

SEM was performed to examine the morphology of cells (Figure 11). Cells grown on the flat surface and 10 nm nanodot arrays exhibited flat and extended conformation during the course of 5 days. Cells grown on 50 nm nanodot arrays showed more extended morphology and apparently larger surface area for each cell compared to those cultured on flat surfaces. Cells grown on 100 nm nanodot arrays exhibited distorted morphology with reduced cell adhesive area. The apoptosis-like appearance and reduction in surface area are most enhanced for cells seeded on the 200 nm nanodot arrays.

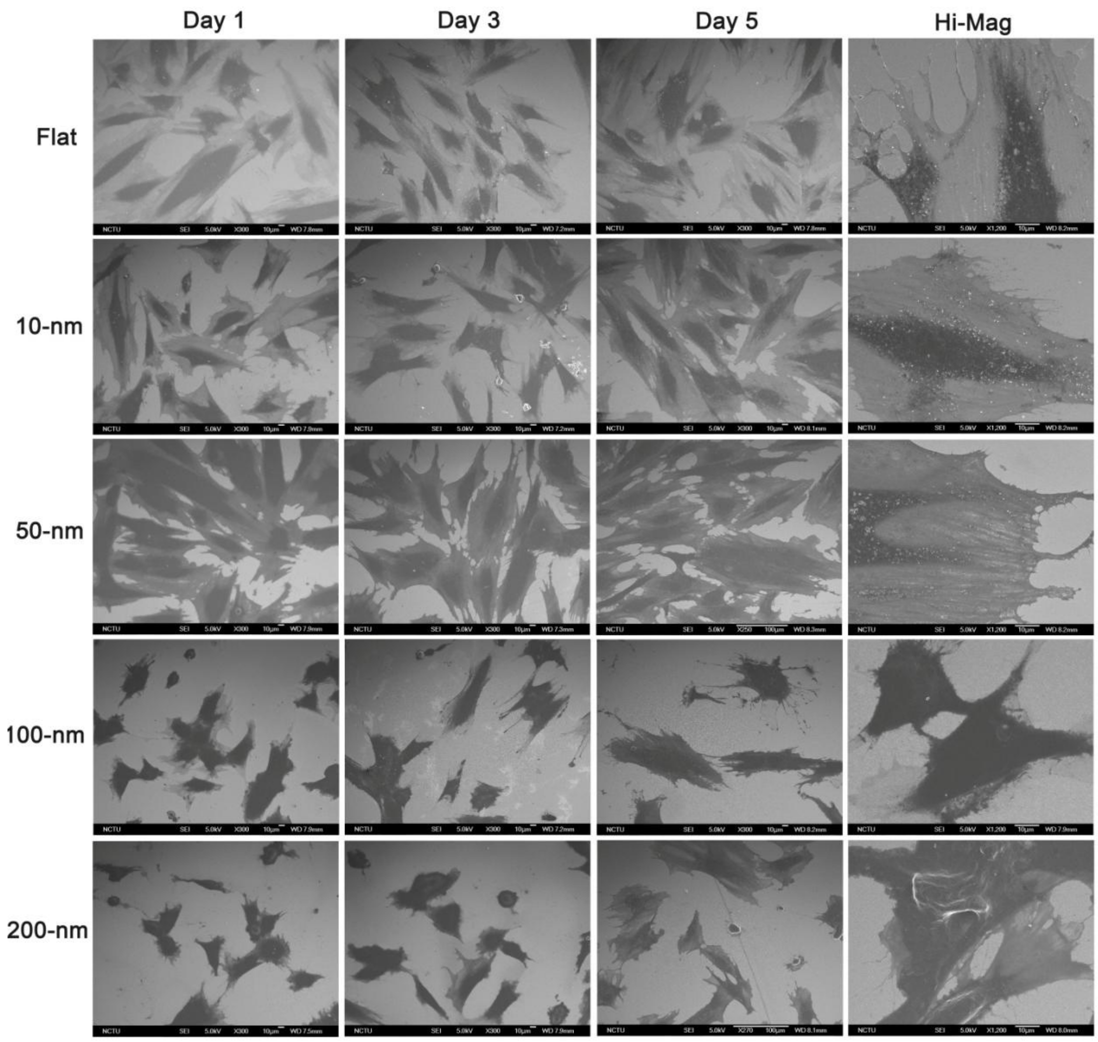

Figure 11 *Morphology of H9c2 cardiomyoblasts cultured on nanodot arrays using SEM. H9c2 cells are grown on flat, 10-, 50-, 100-, and 200 nm nanodot arrays for either 1, 3, or 5 days. High magnification SEM images (Hi-Mag) show lamellipodia present in cells cultured on flat, 10-, 50-, 100-, or 200 nm nanodot arrays for 3 days. Scale bar = 10 μm.*

The morphology of cells clearly varied when cultured on arrays of differently sized nanodots. The variation in morphology also depended on incubation time. The surface area of cells grown on nanodots was measured and compared to that of cells grown on flat surfaces (Figure 12). On day 1, a 2-fold increase in surface area for cells grown on 50 nm nanodots was observed relative to flat surfaces. On day 3, a significant increase in the surface area of cells cultured on 10- and 50 nm nanodot arrays was observed. The increase in surface area was not present on day 5, probably due to the saturation of cells grown on the culture dish. However, on day 5, cells grown on 100 nm nanodot arrays began to show a significant reduction in size.

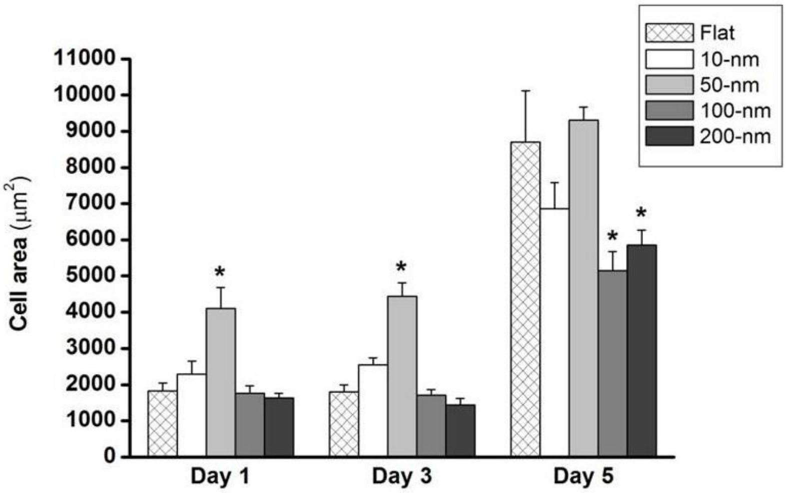

Figure 12 *Time course experiments to determine the dependence on nanotopography of cell spreading area of H9c2 cardiomyoblasts. Cardiomyoblasts seeded on nanodot arrays of various sizes were harvested after 1, 3, or 5 days culture. Plot of cell spreading area versus dot size. Cell spreading area was determined using SEM images of 50 cells per condition. The mean ± SD from at least 3 experiments is shown. *p<0.05 when compared with flat control surfaces.*

Focal adhesion, reflected by the attachment of filopodia and lamellipodia to the surface indicates healthy growth of cultured cells. SEM images showed that the lamellar body of the migrating cells seeded on 50 nm nanodot arrays exhibited wide and thick features (Figure 11). Cells seeded on flat surfaces and 10 nm nanodot arrays showed comparable lamellipodia. However, the cells seeded on 100 nm and 200 nm nanodos arrays are mounted with smaller size and narrow lamellipodia.

In summary, cells seeded on 50 nm nanodots showed the most extended morphology, including the largest surface area, most extended lamellipodia, and fastest growth rate. Cells grown on flat surfaces remained stable in the culture dish, while apoptosis-like growth and a significant reduction in the surface area were observed in cells cultured on the 100- and 200 nm nanodot arrays.

3.3.3Cell adhesion and cytoskeletal organisation of cardiomyoblasts

Topography and surface chemistry may share a common pathway to direct cell behaviour. Cell adhesion is mediated through focal adhesions involving receptor-ligand binding [109]. To evaluate the role of adhesion molecules in nanotopography-induced apoptosis-like events, we immunostained cells grown on nanodot arrays for vinculin and actin filaments (Figure 13). Vinculin is a membrane-bound cytoskeletal protein located in focal adhesion plaques that is involved in linking integrin adhesion molecules to the actin cytoskeleton. Vinculin staining indicated the formation of focal adhesions. Vinculin staining was widely distributed within cells grown on flat surfaces, 10 nm nanodot arrays, and, most prominently, 50 nm nanodot arrays. The amount of vinculin staining decreased or nearly vanished in cells grown on 100- or 200 nm nanodot arrays, respectively. Well-organised actin filaments were visible in cells grown on flat, 10-, and 50 nm nanodot arrays. This tight cytoskeletal arrangement was gradually lost and entirely disappeared for cells grown on 100- and 200 nm nanodot arrays, respectively.

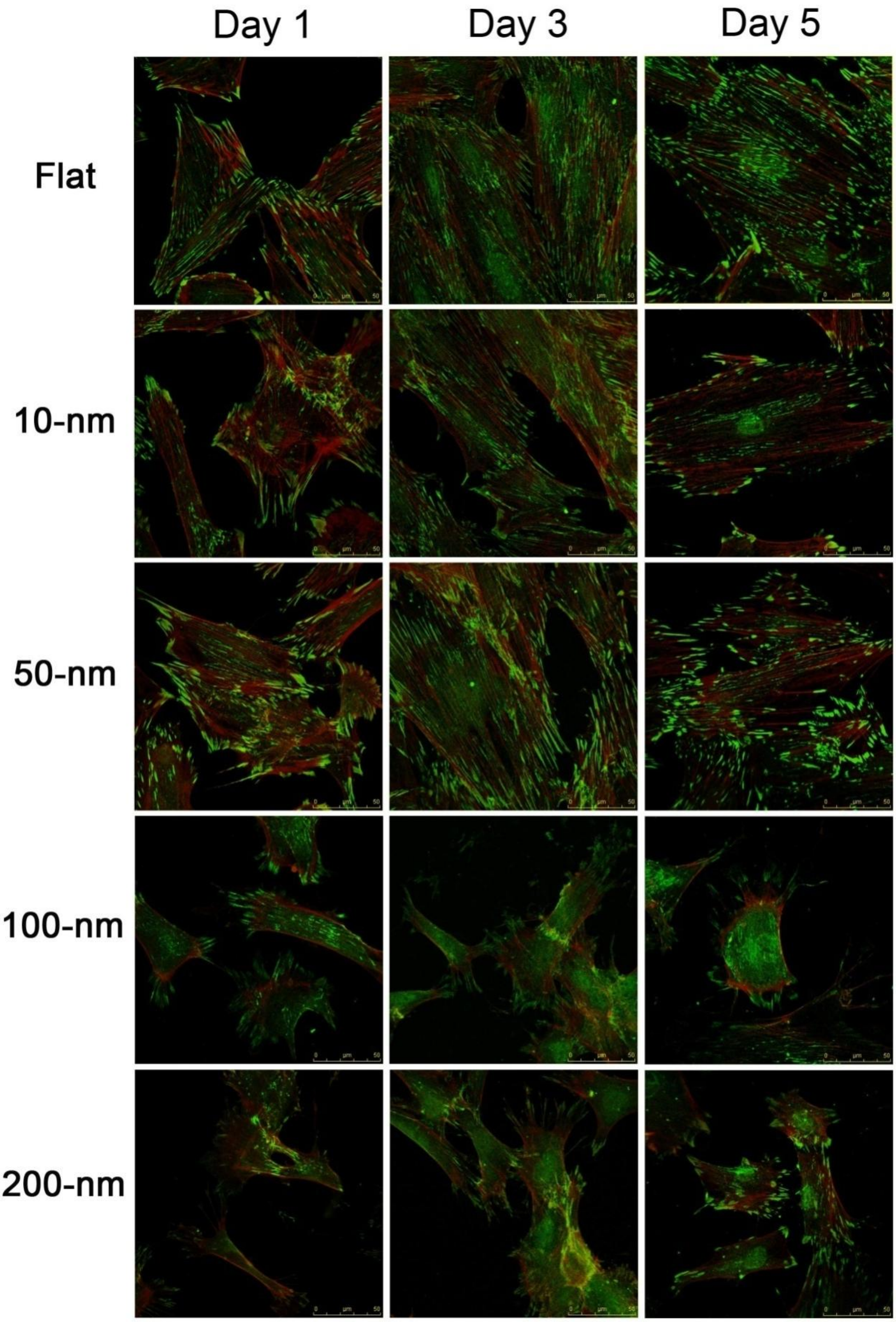

Figure 13 *Immunofluorescent staining shows distribution of vinculin (green) and actin filament (red) in H9c2 cells cultured on nanodot arrays. H9c2 cells were seeded on flat, 10-, 50-, 100-, and 200 nm nanodot arrays for 1, 3, or 5 days. Scale bar = 50µm.*

Immunostaining indicated that nanodots smaller than 50 nm in diameter promoted protein expression related to cell adhesion and cytoskeletal organisation in cardiomyoblasts. Optimal adhesion occurred at 50 nm. Nanodots 100- and 200 nm in diameter reduced the formation of focal adhesions and inhibited the organisation of the cytoskeleton.

3.3.4Expression of genes associated with cardiovascular function in cardiomyoblasts grown on varied nanotopographies

Heat shock proteins (Hsp) are involved in the cell response of heart disease. Hsp90 has been identified as a signalling molecule involved in the activation of all isoforms of nitric oxide synthase (iNOS). The present study showed that Hsp90, induced by mild heat shock treatment, can activate nitric oxide synthase enzymes (NOS) in cardiac H9c2 cells and result in production of nitric oxide (NO), a regulator of cell respiration [110]. The regulation of cellular respiration is directly related to many cardiovascular diseases. Periannan Kuppusamy’s group has shown that the induction of Hsp90 during heat shock can activate NOS and increase NO production, thereby inhibiting respiration in cardiac H9c2 cells [111]. Quantitative PCR was performed to determine the levels of Hsp expression corresponding to various nanotopographies. As shown in figure 14, mRNA levels of Hsp90 were significantly upregulated in cells cultured on 100 nm nanodot arrays. Expression levels of Hsp70, Hsp60, and Hsp27 remained unchanged. Collectively, these data indicate that a stress response was induced in cells cultured on the 100 nm nanodot arrays.

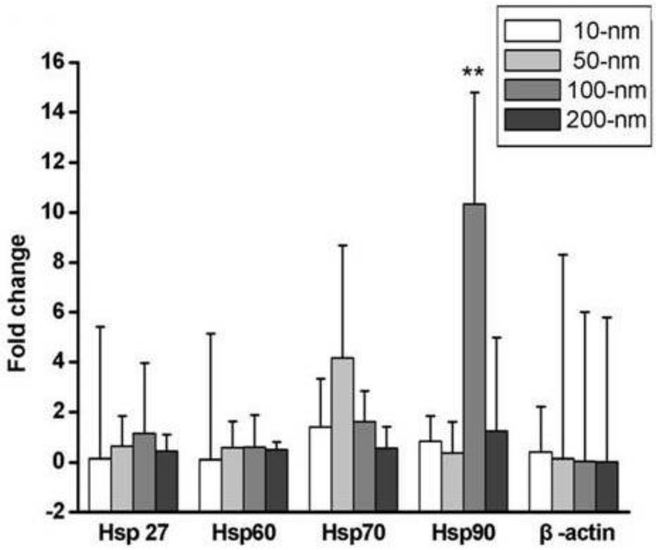

Figure 14 *qPCR of genes associated with heat shock in H9c2 cardiomyoblasts. H9c2 cells were cultured on flat, 10-, 50-, 100-, and 200 nm nanodot arrays for 3 days before qPCR was performed. The mean ± SD from at least 3 experiments is shown. *p<0.05 and **p<0.01 when compared with flat control surfaces.*

Receptor activity–modifying proteins 2 and 3 (RAMP-2 and -3) are associated with increased vascular smooth muscle cell migration [112]. The expression of RAMP-2 or RAMP-3 mediates the inhibitory effect of adrenomedullin on cell migration. The high-affinity adrenomedullin receptor involved in the pathogenesis of cardiovascular diseases is composed of RAMP-2 and RAMP-3 [99]. Thus, RAMPs are key determinants of adrenomedullin-mediated effects on cell migration and are essential for angiogenesis and vascular integrity [113]. The mRNA levels of RAMP-2 and -3 increased for cardiomyoblasts seeded on 50- or 100 nm nanodot arrays (Figure 15). Nanotopography appeared to upregulate expression of RAMPs and control cell migration and the angiogenesis-like phenomenon.

Genes associated with apoptosis were also examined. The proapoptotic protein Bax plays an important role in cardiomyocyte cell death [114]. Overexpression of the anti-apoptotic Bcl-2 gene has been found in cardiac fibroblasts, which are well known to resist most situations that compromise cell survival [115]. Significant induction of

Bcl-2 expression limits uncontrolled cell death [116]. The two genes, Bax and Bcl-2, play key roles in mitochondrial permeability and, thus, apoptosis [117]. The mRNA expression profile of Bcl-2 and Bax observed in H9c2 cardiomyoblasts cultured on different nanotopographies were determined using qPCR (Figure 15). The lack of an apparent difference in Bcl-2 and Bax expression indicated that these two genes were less correlated to the topography-induced apoptotic pathways.

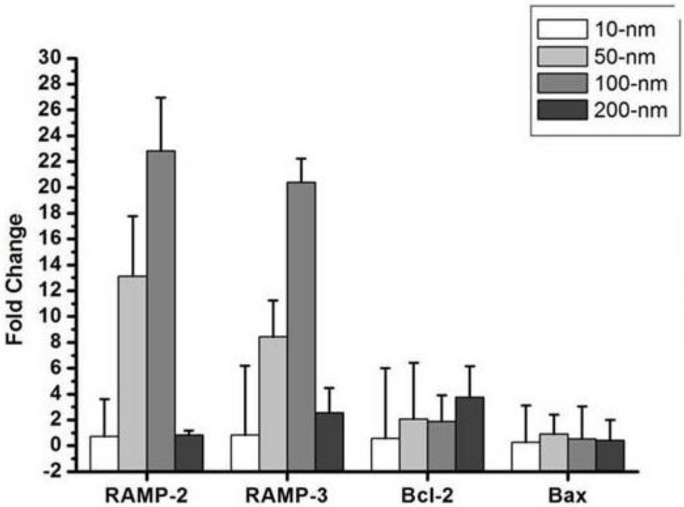

Figure 15 *qPCR of genes associated with apoptosis in H9c2 cardiomyoblasts. H9c2 cells were cultured on flat, 10-, 50-, 100-, and 200 nm nanodot arrays for 3 days before qPCR was performed. The mean ± SD from at least 3 experiments is shown. *p<0.05 and **p<0.01 when compared with flat control surfaces.*

The characteristic features of cardiac hypertrophy include increased cell area, enhanced cytoskeletal organisation, elevated cardiac gene expression, and upregulated atrial natriuretic factor (ANF) and beta myosin heavy chain (β-MHC) [118]. PAI-1 inhibits extracellular matrix-degrading metalloproteinases and promotes fibrosis in neonatal rat cardiomyoblasts and H9c2 rat cardiomyoblasts [22]. The transcription factor GATA-4, a master regulator of cardiac genes, has been implicated in both the transcriptional activation of genes encoding ANF and contractile proteins and the sarcomeric reorganisation response to hypertrophic stimulation [119].

We measured the expression of hypertrophy-associated genes, including PAI-1, β-MHC, GATA-4, and ANF, in cardiomyoblasts cultured on various nanotopographies. As shown in Figure 16, the mRNA levels of PAI-1 and β-MHC were significantly enhanced in cells cultured on 50- and 100 nm nanodot arrays. The expression levels of GATA-4 and ANF remained unchanged.

The mRNA expression levels of PAI-1 and β-MHC increased in cardiomyoblasts that were seeded on 50- and 100 nm nanodot arrays. Arrays of 50- and 100 nm-diameter nanodots may promote hypertrophic and fibrotic processes in cultured cardiomyoblasts.

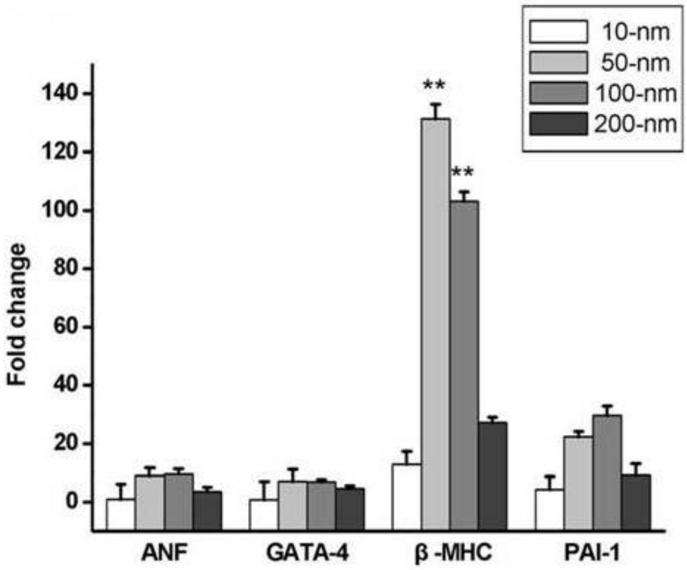

Figure 16 *qPCR of genes associated with hypertrophy, and fibrosis in H9c2 cardiomyoblasts. H9c2 cells were cultured on flat, 10-, 50-, 100-, and 200 nm nanodot arrays for 3 days before qPCR was performed. The mean ± SD from at least 3 experiments is shown. *p<0.05 and **p<0.01 when compared with flat control surfaces.*

3.3.5 Western blotting and confirmation of the topological control of PAI-1 and vinculin expression

Nanotopography controls the cell adhesion and cellular function of cardiomyoblasts. Western blots were performed to validate the expression of vinculin and PAI-1 proteins (Figure 17a). Cell spreading and migration occur though the binding of cell surface integrin receptors to extracellular matrix adhesion molecules. Vinculin is associated with focal adhesions and adherens junctions, both of which connect actin filaments and crosslinkers between the external medium, plasma membrane, and actin cytoskeleton [120]. In the immunofluorescence experiments, vinculin staining reached maximum for cells cultured on 50 nm nanodot arrays. Based on western blot results, the highest level of expression occurred in cells cultured on 50 nm nanodot arrays (Figure 17b). The levels of PAI-1 were enhanced significantly in cardiomyoblasts seeded on 50 nm nanodot arrays (Figure 17c). Although the 50 nm nanodot array surface enhanced cell growth and adhesion, it also promoted the risk of hypertrophic stimulation and fibrosis in cardiomyoblasts.

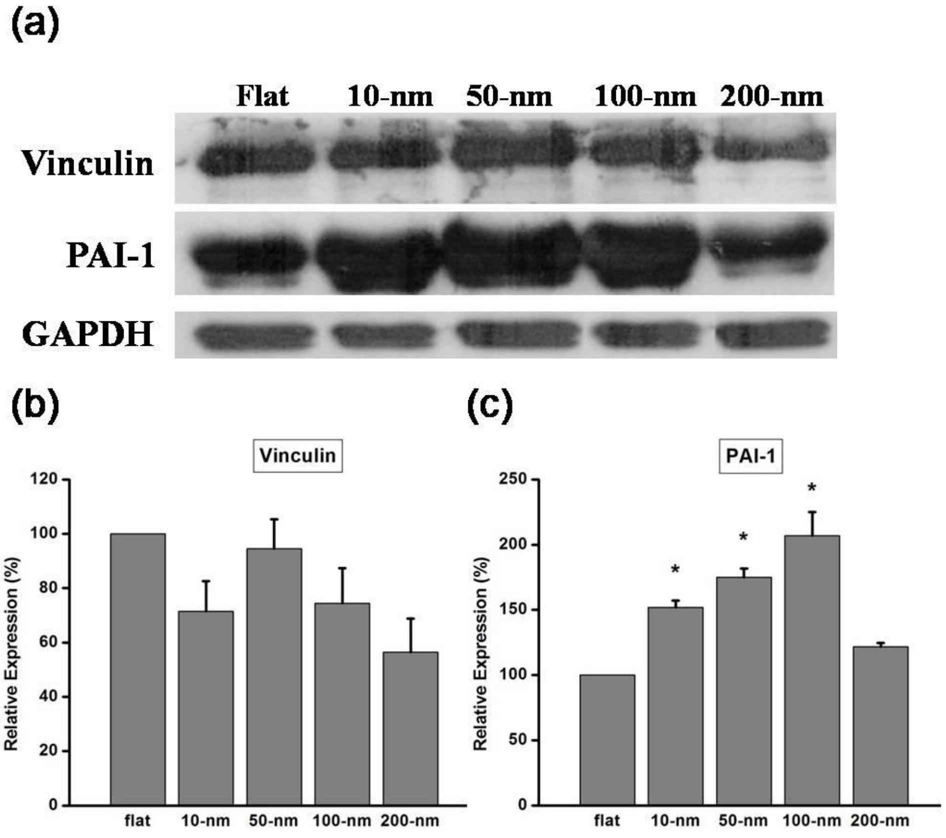

Figure 17 *Protein expression of H9c2 on nanodot arrays (a) Western blots analysis of vinculin and PAI-1 for H9c2 cells cultured on nanodot arrays. Cardiomyoblasts were*

*collected after 3 days culture. (b) Relative density of vinculin expression versus nanodot size. (c) Relative density of PAI-1 expression versus nanodot size. The densitometric analysis of each band was performed and relative density calculated using expression of GAPDH as a control. The mean ± SD from at least 3 experiments is shown. *p<0.05 when compared with flat control surfaces.*

3.4 Optimization for the biocompatibility of dental implants using nano-structures/MG 63 osteoblasts model system

3.4.1The topology controlled the viability, apoptosis, and adhesion of MG63 osteoblasts

MG63 osteoblasts were cultured on fabricated nanodot arrays at densities of 1,000 to 5,000 cells per square centimeter. The cells were harvested 3 days after seeding. SEM was performed to examine the viability and apoptosis-like morphology of the cells (Figure 18). The number of focal adhesions is the hallmark for cell attachment and can be evaluated by immunostaining against vinculin. The organization of the cytoskeleton was visualized by immunostaining for the actin filament bundles (Figure 19). To evaluate the size effect of the nanodot arrays, the percent viability, the percent apoptosis, the number of focal adhesions, and the number of microfilament bundles were drawn against the dot diameters

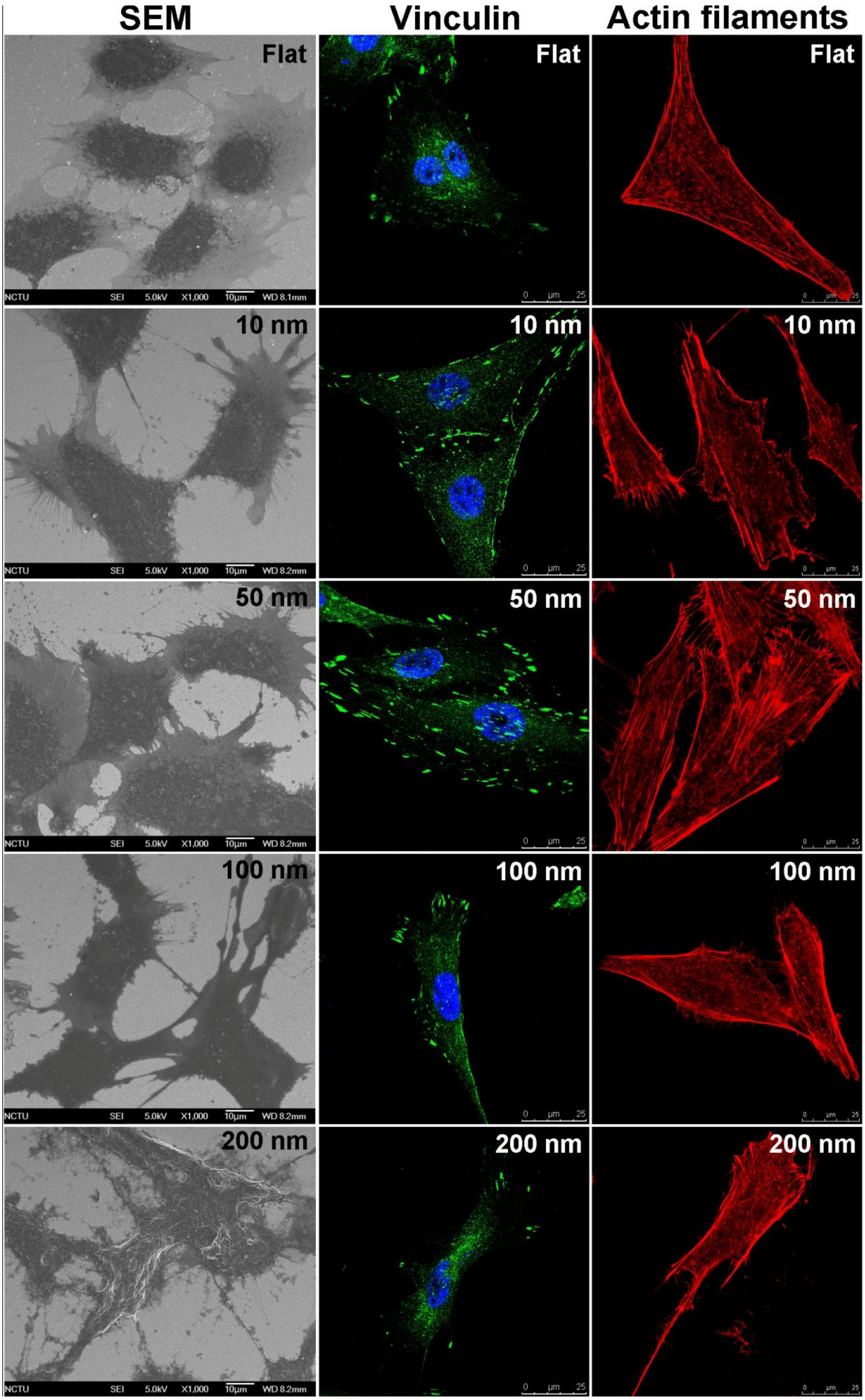
SEM
Vinculin
Actin filaments
Flat
Flat
Flat
NCTU SEI 5.0kV X1,000 10µm WD 8.1mm
0 µm 25
0 µm 25
10 nm
10 nm
10 nm
NCTU SEI 5.0kV X1,000 10µm WD 8.2mm
0 µm 25
0 µm 25
50 nm
50 nm
50 nm
NCTU SEI 5.0kV X1,000 10µm WD 8.2mm
0 µm 25
0 µm 25
100 nm
100 nm
100 nm
NCTU SEI 5.0kV X1,000 10µm WD 8.2mm
0 µm 25
0 µm 25
200 nm
200 nm
200 nm
NCTU SEI 5.0kV X1,000 10µm WD 8.2mm
0 µm 25
0 µm 25

Figure 18 Modulation for the growth of and the formation of focal adhesions by MG63 cells by nanodot arrays. On the left are SEM images of cells seeded on the nanodot arrays for 3 days. Immunostaining against vinculin is performed to evaluate the formation of focal adhesions. Actin filament staining is performed to visualize the organization of the cytoskeleton by phalloidin. The fluorescence images are taken with a confocal microscope.

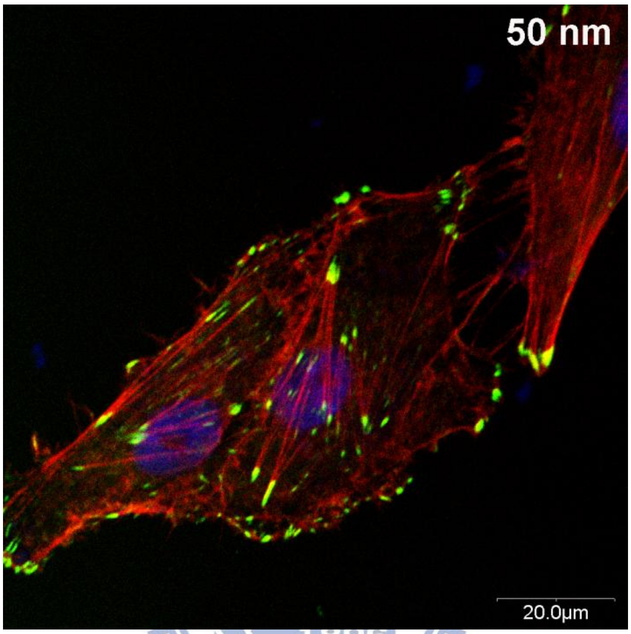

Figure 19 *Vinculin (green), actin filament (red), and cell nucleus (blue) high magnification fluorescence image of MG63 cells after 3 days culture on 50 nm nanodot array. Cells exhibited well-defined actin filaments and focal adhesion with vinculin in the cytoplasm.*

The cell viability was closely associated with the surface topology. The viability of MG63 cells initially increased when the diameter of the nanodots increased. The viability reached a maximum at a nanodot diameter of approximately 50 nm but dropped dramatically for the 100 nm and 200 nm nanodot arrays. The viability reached a maximum of +143.9 % at a dot diameter of 48.79 nm (Figure 20). A significant decrease of the viability was observed for the cells grown on the 200 nm nanodots (65 % viability).

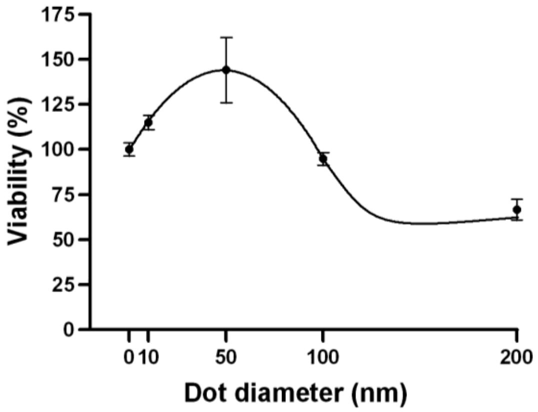

Figure 20 *The cell viability versus dot diameters for cells cultured on nanodot arrays. Cells were cultured on the nanodot arrays for 3 days. The percentage values relative to the cells that were cultured on a flat surface (0 nm) were calculated and plotted against the nanodot diameter.*

Decreased viability occurred with MG63 cells seeded on larger nanodots. The decrease in cell viability is very likely due to programmed cell death. Cells that underwent apoptosis exhibited an abnormal morphology that was identified in the SEM images. The percentages of apoptotic cells versus dot diameters were plotted for the MG63 cells. Minimal apoptosis occurred when the dot diameter approached 50 nm (Figure 21). The cells started to show thickening and mounting when the dot size was larger than 100 nm; considerable thickening and mounting were observed when the dot size was 200 nm. On the contrary, cells grown on a flat surface and on 10 nm and 50 nm nanodot arrays were flat and extended. Cells grown on 50 nm nanodots exhibited the most extended morphology.

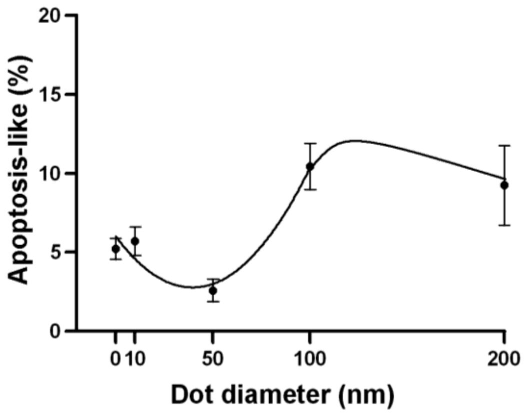

Figure 21 *The apoptosis-like events versus dot diameters for cells cultured on nanodot arrays. Cells were cultured on the nanodot arrays for 3 days. The percentage values relative to the cells that were cultured on a flat surface (0 nm) were calculated and plotted against the nanodot diameter.*

The organization of the cytoskeleton is an important index for cell growth. Although there is no quantitative measurement for cytoskeletal organization, the number of cytoskeletal fibers is a well-recognized estimation. Cells grown on a flat surface and on 10 nm, 50 nm, and 100 nm nanodots exhibited well-defined actin filaments in the cytoplasm. However, there was a visible loss of actin filament bundles in cells grown on the 200 nm nanodots (Figure 22).

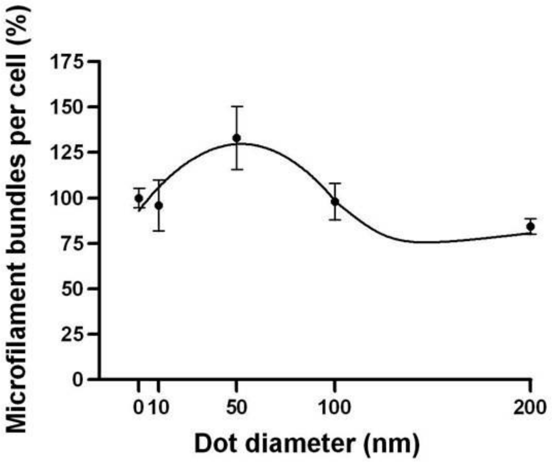

Figure 22 *The microfilament bundles versus dot diameters for cells cultured on nanodot arrays. Cells were cultured on the nanodot arrays for 3 days. The percentage values relative to the cells that were cultured on a flat surface (0 nm) were calculated and plotted against the nanodot diameter.*

The formation of focal adhesions is a hallmark for the proper attachment of cells and can be estimated by the degree of vinculin staining. The formation of focal adhesions versus the dot diameter exhibited a trend that was similar to that for the viability versus the dot diameter. There was an initial increase of focal adhesion formation that gradually decreased when the nanodot diameter exceeded 50 nm (Figure 23). The maximum number of focal adhesions occurred with a dot diameter of 59.4 nm; at this diameter, there was a 73.2 % increase in the number of focal adhesions compared to those formed by cells cultured on a flat surface (Table 2).

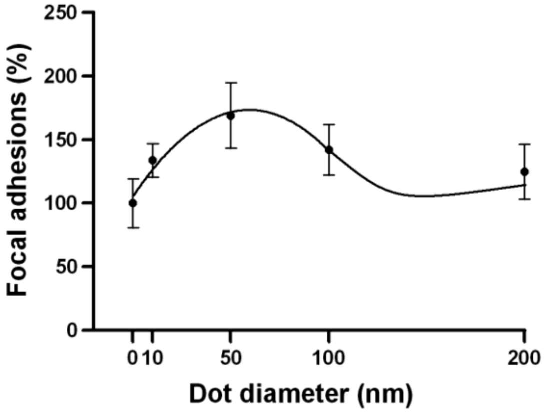

Figure 23 *The focal adhesions versus dot diameters for cells cultured on nanodot arrays. Cells were cultured on the nanodot arrays for 3 days. The percentage values relative to the cells that were cultured on a flat surface (0 nm) were calculated and plotted against the nanodot diameter.*

3.4.2The mineralization of MG63 cells was associated with the nanotopology

The mineralization process is a hallmark for the function of osteoblasts. To investigate the modulation of the mineralization process, MG63 cells were cultured onthe integrated nanodot array device for 7 days. Mineralization in cell culture monolayers has been determined using quantitative methods with von Kossa and Alizarin Red S staining. The phosphate ion precipitation was visualized as dark crystals following von Kossa staining. The calcium deposition was stained bright red following Alizarin Red S staining. By von Kossa staining, a high density of nodular phosphate ion precipitation was identified in cells grown on the 50 nm nanodots (Figure 24). A 54.5 % increase in phosphate ion precipitation occurred in cells cultured on 46.3 nm nanodots compared to cells grown on a flat surface (Table 2). By Alizarin Red S staining, a high density of nodular calcium deposition was identified in cells grown on 10 nm and 50 nm nanodots (Figure 25). The quantification of mineralization by Alizarin Red S staining indicated a 44.6 % increase in mineral contentin cells cultured on 46.7 nm nanodots (Table 2). The nanotopography should provide biomimetic surfaces that support mineral formation and guide bone mineralization [12].

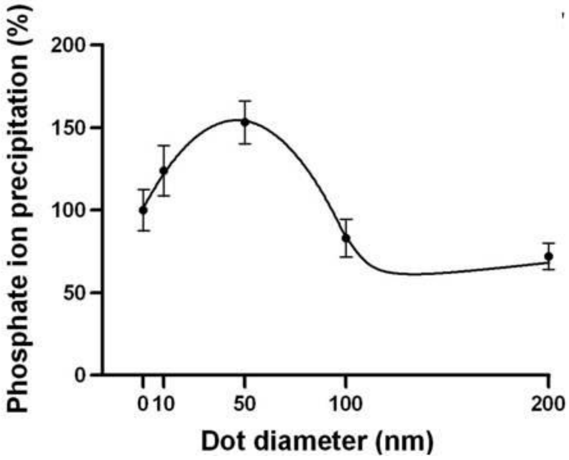

Figure 24 *Phosphate ion precipitation to detect the mineralization of cultured MG63 cells using von Kossa staining. A correlation between the mineralization and the size of the nanodot arrays was observed. The optimal size was obtained at 46.3 nm with a maximal calcium deposition of 54.5 %.*

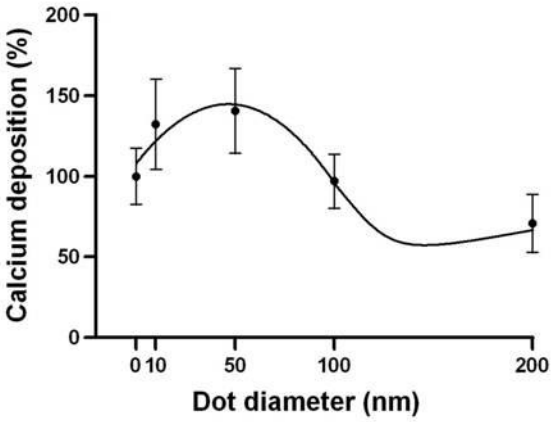

Figure 25 *The mineral calcium deposition of cultured MG63 cells visualized with Alizarin Red S staining. MG63 cells were seeded onto nanodots and grown for 7 days. (a) Flat, (b) 10 nm, (c) 50 nm, (d) 100 nm, (e) 200 nm. The correlation between the degree of mineralization and the size of the nanodot arrays was observed. The relative mineralization is calculated relative to that of a flat surface. The optimal size was obtained at 46.7 nm, and the maximal calcium deposition degree is 44.6 %.*

Table 2 *Summary for the optimal size of nanodots and relative improvements derived from the in vitro survey of nanotopography*

Cell characterization	**Optimal size (nm)**	**Relative improvement (%)**
Viability	48.8	+43.9
Apoptosis-like cells	39.6	-97.2
Microfilament bundles	52.2	+29.7
Focal adhesions	59.4	+73.2
Phosphate ion precipitation	46.3	+54.5
Calcium deposition	46.7	+44.6

“+” Indicates the amount of enhancement relative to cells grown on a flat surface.

“-” Indicates the amount of reduction relative to cells grown on a flat surface.

3.4.3The nanostructured surfaces of dental implants

Topology on the nanoscale affects cell growth and function. Table 2 summarizes our investigation for the optimized condition of osteoblasts. Nanodots of diameters ranging from 46 nm to 60 nm provided the most biocompatible environments for growth and function. It would be intriguing if the *in vitro* outcomes could benefit the clinical applications in the design of dental implants. The utility of the nanostructure was further evaluated by the clinical studies. In the clinical studies, four commercially available dental implants were employed: a calcium phosphate (CaP)-treated implant (A and B), a titanium plasma coated implant (C) and an uncoated implant (D).

Electron microscopy was performed to examine the microstructure and nanostructure surfaces of the implants (Figure 26). Implant A contains scattered microscale furrows approximately 1 μm in height with a density much lower than that of the other implants; it contains approximately 20 nm nanodots sparsely distributed with crystal-to crystal distances of 173.2 ± 39.1 nm. Implant B showed a relatively flat micro-landscape with rounded agglomerates of approximately 10 nm to 20 µm in diameter and less than 5 μm in height. Implant B also presented nanodots that were closely packed on the surface of the implant. The particles are homogeneous in size with an average diameter of approximately 42 nm. Implant C, one of the non-coated implants, contains unevenly scattered hills and valleys at the microscale. There were no nanoscaled hills; however, nanoscale cracks of approximately 181 nm in diameter were observed. The cracks are shallow (less than 10 nm). The nanotopography of this implant may be considered to be flat. Implant D exhibited microscaled furrows of approximately 1 micron in height. Nanoparticles with an average diameter of approximately 31 nm were sparsely scattered on the surface with dot-to-dot distance longer than 200 nm. The dimensions for the nanostructures on the surface of each type of implant are summarized in Table 3. It should be noted that Implant B contained large area of close-compacted nanodots in a landscape resembling the 50 nm nanodot arrays in our model system.

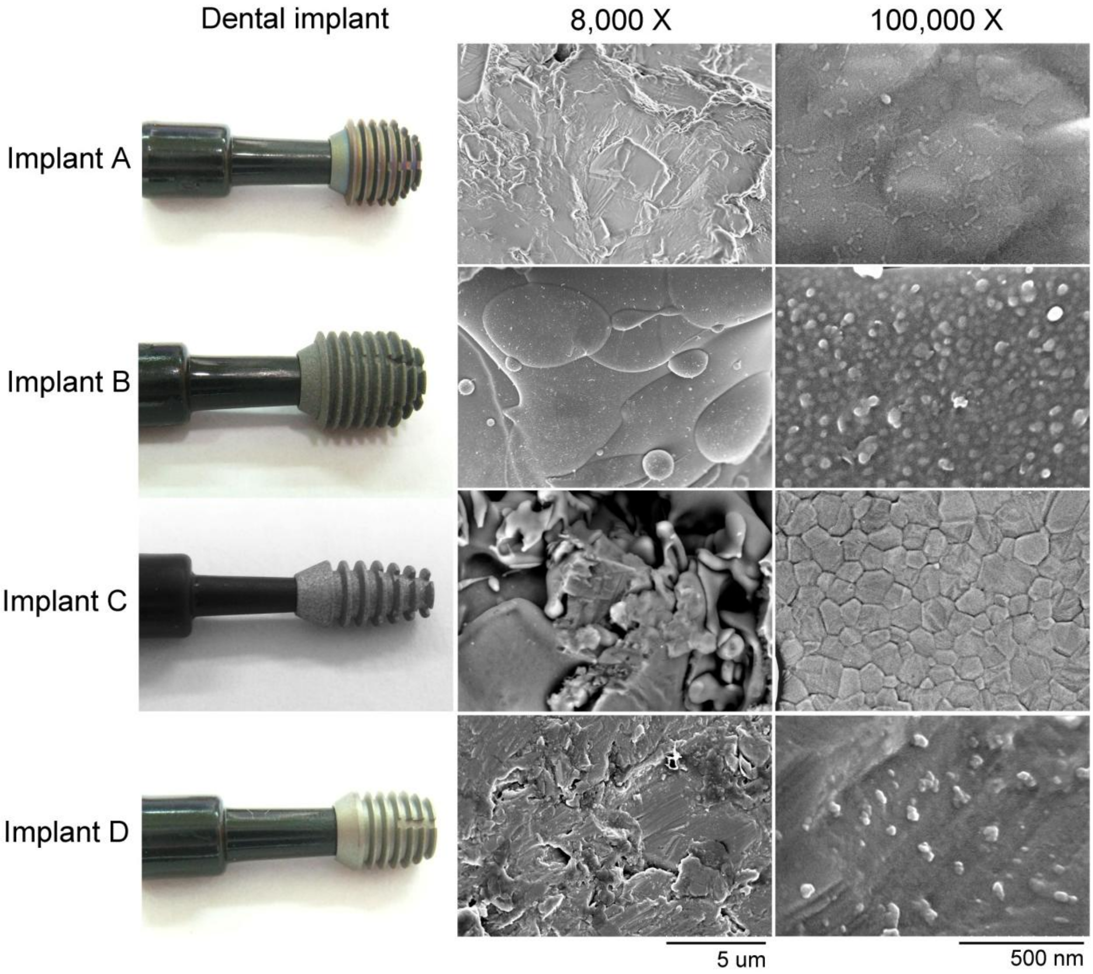

Figure 26 *The dental implants and their surface structures. On the left are photographs of 4 types of dental implants. The corresponding SEM images show the micro-(8,000X) and nano-(100,000X) structures of the dental implants.*

Table 3 *Characterization of the surface structures and chemistry for dental implants*

Implant identity	**Diameter of nanostructure**[a]	**Description of landscape**	**Surface chemistry (fabrication)**
A	19.6 ± 3[b]	Random crystals	CaP (crystalline deposition)
B	41.9 ± 5[c]	Ordered dots	CaP (plasma spray)
C	181.3 ± 51	Shallow cracks	Ti (plasma spray)
D	30.6 ± 18[d]	Scattered dots	Ti

[a] Values are Mean ± SE (nm).

[b] The crystal-to-crystal distance is 173.2 ± 39.1 nm

[c] The dot-to-dot distance is 49.3 ± 9.1 nm

[d] The dot-to-dot distance is 242.6 ± 60.2 nm

3.4.4Cell growth on the dental implant in vitro

MG63 osteoblasts were grown on 4 types of dental implants for 7 days and examined by SEM to observe the cell morphology (Figure 27). Diversified cell morphologies were observed. For the CaP-coated implants, MG63 cells were flat and extended on Implant B. A number of filopodia extending beyond the leading edge of the lamellipodia indicated the migration of viable MG63 cells. However, on Implant A, the cells exhibited a spindle-like shape, a mounted morphology, and the culture started to separate into small cell bodies. The cell morphology indicated that the MG63 cellswere undergoing apoptosis on Implant A.

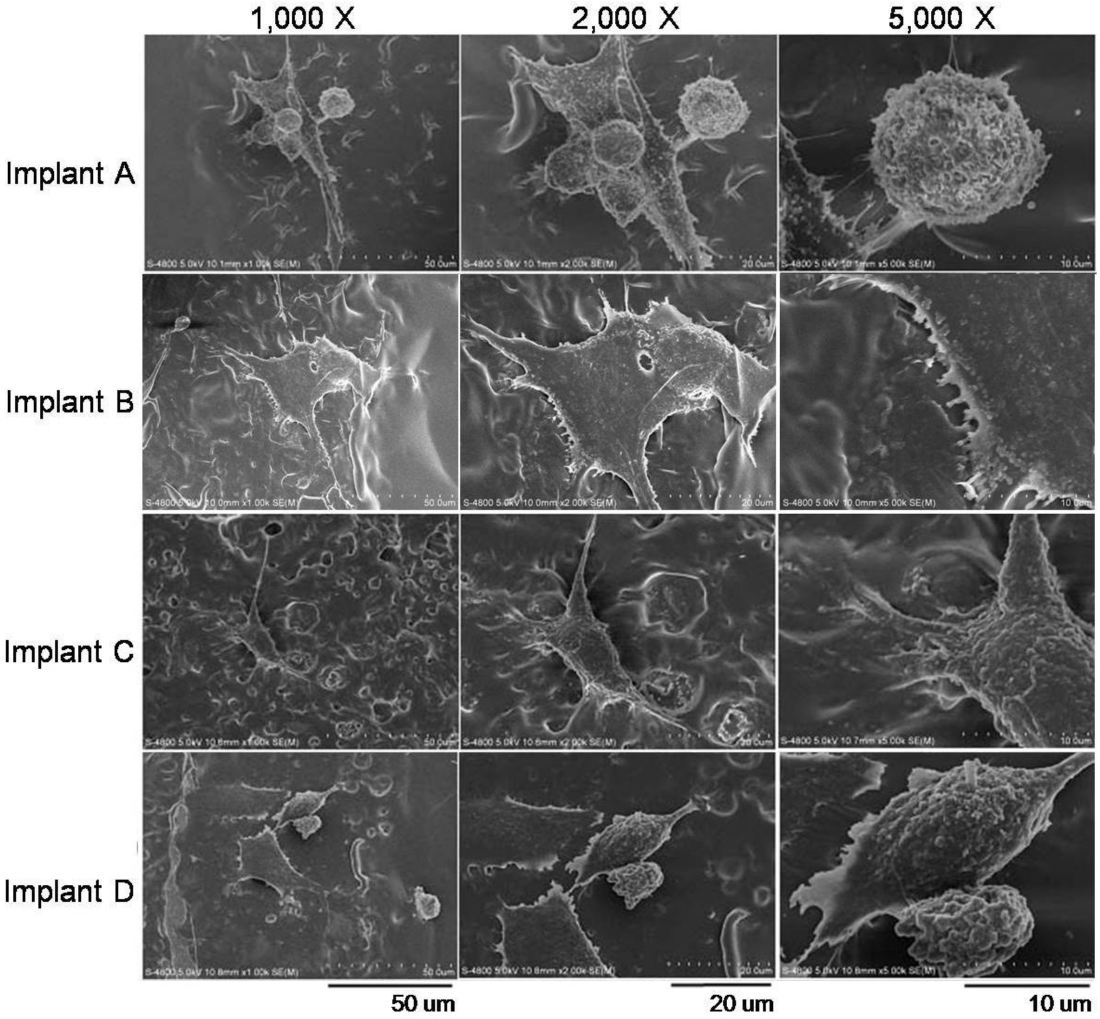

Figure 27 *SEM images for MG63 cells grown on dental implants. The cells were grown on implants for 7 days and then harvested. The morphology of the cells indicated healthy growth for Implant B. The cell morphology in Implant A indicated apoptosis-like growth.*

On Implant C, spindle-like cells with few filopodia extending beyond the lamellipodia indicated the migration of viable MG63 cells. The cells are viable and migrateon Implant C. The simultaneous growth of migrating cells and apoptotic-like cells was observed on Implant D. It is probably due to the scattered distribution of the 50 nm nanodots. The cells exhibited proper adhesions with the 50 nm dot-to-dot distance; however, when the dot-to-dot distance was larger than 100 nm, the cells started to struggle for adhesion and exhibited growth-retardation. The co-existence of migrating cells and apoptosis-like cells in close vicinity is a reflection of the complicated topologic surface structures.

3.4.5Clinical survey for dental implants

During a 2-year period (2007–2009), 44 patients (18 male, 26 female) between 33 and 82 years of age (mean: 55 years) received dental implants. The time for the stabilization of the implants was plotted. Among all of the patients, 7 patients received multiple types of implants (Table 4). For the smoking group, Implants B and C exhibited shorter durations for the implant to stabilize in the bone: 101.8 ± 23.0 days for Implant B and 101.3 ± 19.1 days for Implant C. Implant A performed poorly with a stabilization time of 239.3 ± 33.4 days. For the nonsmoking group, Implant B performed the best with a stabilization time of 108.5 ± 16.7 days. Implants A and C were undistinguishable with stabilization times of 132.8 ± 21.0 days and 133.9 ± 12.9 days, respectively. The longest stabilization period occurred with Implant D (162.5 ± 48.9 days) (Figure 28). Various implants within the same patient may provide the opportunity to justify the clinical data (Table 4). In general, within the same patient, the duration of the stabilization time corresponded to Implant B < Implant C < Implant D/A.

Table 4 *The duration of stabilization for individual dental implant in patients receiving multiple implants*[a]

Patient identity	Implant A	Implant B	Implant C	Implant D
1 (Smoker)	98		98	98
2 (Smoker)	360	60	60	
3 (Smoker)	255	210	120	
4 (Smoker)	270	83	165	
5 (Nonsmoker)	180	90	120	
6 (Nonsmoker)	300	75	120	
7 (Nonsmoker)		90	60	360

[a] The number indicates days required for stabilization.

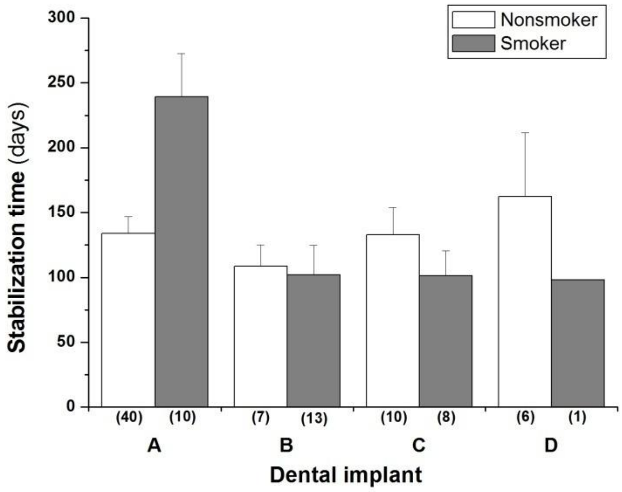

Figure 28 *The stabilization time of the dental implants. Y-axis depicts days of stabilization for corresponding implants. Patients are divided into nonsmoker (blank bars) and smoker (filled bars) groups. The number in the paranthesis indicates number of implants in the same group. Mean values of stabilization time is shown. Error bars represent standard deviation.*

In this study, we evaluated the topologic effects on the growth and function of osteoblastic cell line MG63. MG63 cells were grown on nanodot arrays ranging in diameter from 10 nm to 200 nm. Cell proliferation, morphology, adhesion, cytoskeleton, and mineralization were evaluated. Nanodot diameters ranging from 46 nm to 60 nm provided the optimized condition for the viability, proliferation, cell adhesion, and mineralization of MG63 cells. Nanodots lager than 100 nm retarded the growth and suppressed the functional expression of the cells. A clinical survey was performed using four different types of dental implants: two that were coated with CaP and two that were uncoated. Optimal results occurred with implants with surface nano-structures that were appropriate for cell growth, while a prolonged duration of stabilization occurred with implants with nanostructures that retarded cell growth and function.

3.5 *A nanodevice for rapid modulation of proliferation, apoptosis, invasive ability, and cytoskeletal reorganization in cancer cells*

3.5.1 *Assessment of proliferation, apoptosis, cell adhesion, and cytoskeleton reorganization for cancer cell lines*

To define parameters that modulate the growth state of cells and to assess the cellular response against a varied nanostructured surface, the integrated nanodevice was first placed in the cell culture dish. HELA, C33A, ES2, PA-1, TOV-112D, TOV-21G, MG63, and NIH-3T3 cells were seeded on the device and cultured for three days (Table 5). Among them, NIH-3T3 cells were incorporated as a control cell line for normal fibroblasts. Cell density was counted to examine the viability of cells, and SEM was performed to assess the morphological changes of cells (Figure 29). To evaluate cell adhesion and cytoskeletal reorganization, immunostaining specific to vinculin and actin filaments (microfilaments) was performed (Figure 30 and Figure

31).

Table 5 *Characterization of cell lines used in the current study*

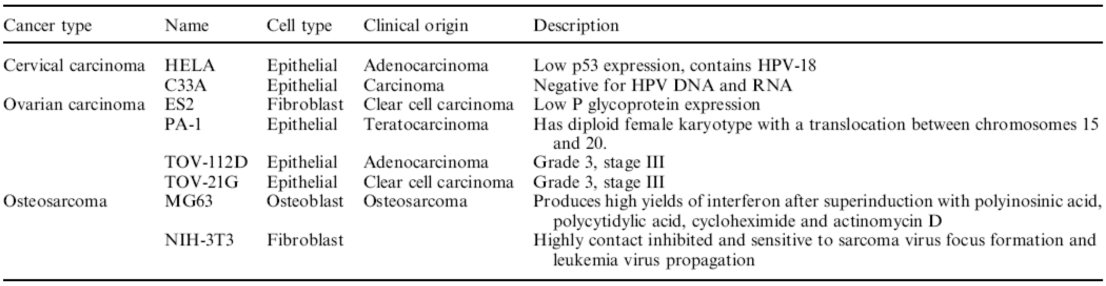

Cancer type	Name	Cell type	Clinical origin	Description
Cervical carcinoma	HELA	Epithelial	Adenocarcinoma	Low p53 expression, contains HPV-18
	C33A	Epithelial	Carcinoma	Negative for HPV DNA and RNA
Ovarian carcinoma	ES2	Fibroblast	Clear cell carcinoma	Low P glycoprotein expression
	PA-1	Epithelial	Teratocarcinoma	Has diploid female karyotype with a translocation between chromosomes 15 and 20.
	TOV-112D	Epithelial	Adenocarcinoma	Grade 3, stage III
	TOV-21G	Epithelial	Clear cell carcinoma	Grade 3, stage III
Osteosarcoma	MG63	Osteoblast	Osteosarcoma	Produces high yields of interferon after superinduction with polyinosinic acid, polycytidylic acid, cycloheximide and actinomycin D
	NIH-3T3	Fibroblast		Highly contact inhibited and sensitive to sarcoma virus focus formation and leukemia virus propagation

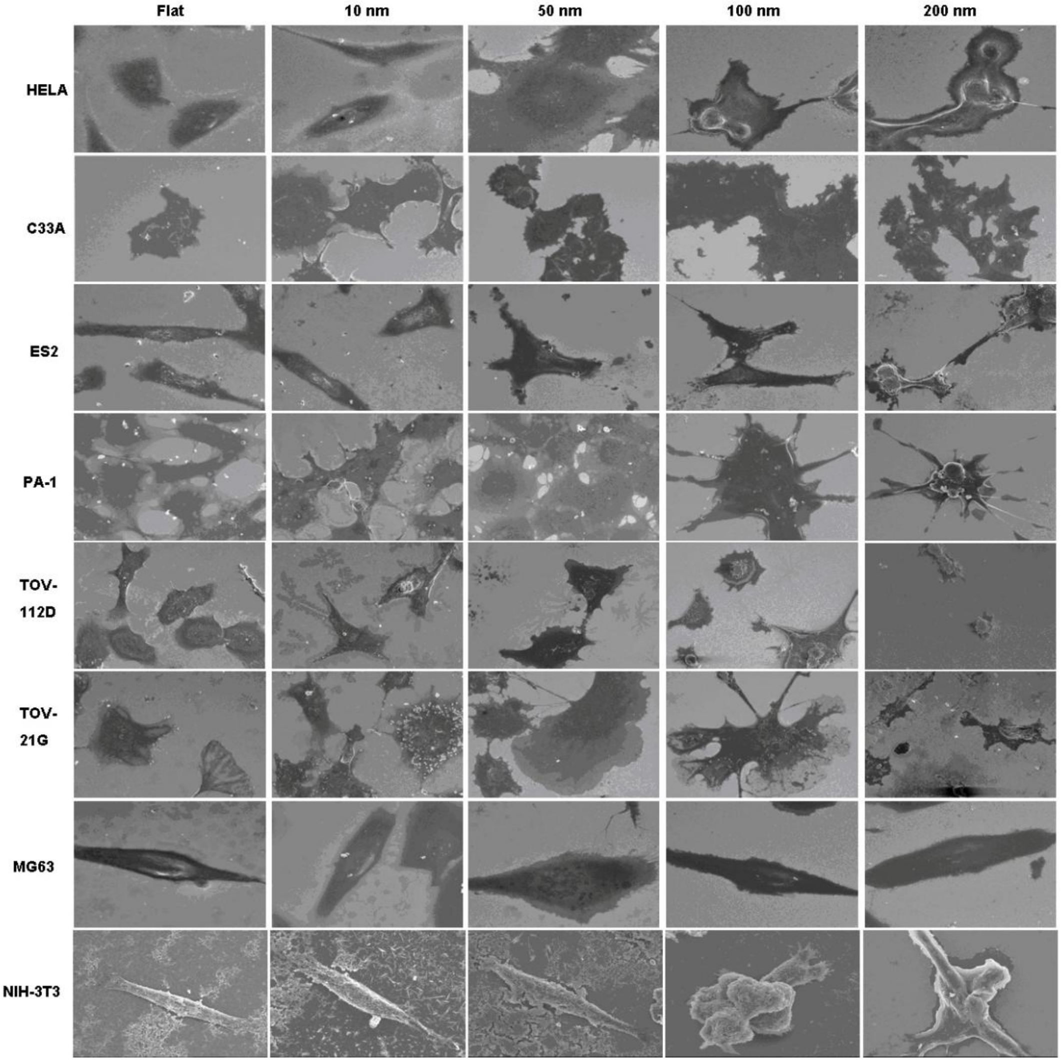

Figure 29 *SEM images of cells seeded on nanodot arrays. HELA, C33A, ES-2, PA-1,*

TOV-112D, TOV-21G, MG63, and NIH-3T3 cells were seeded on a flat silicon surface and a 10 nm-nanodot array (10 nm), 50 nm nanodot array (50 nm), 100 nm nanodot array (100 nm), and 200 nm nanodot array (200 nm). Cells were harvested at 72 hours (day 3) after seeding. Representative SEM images are shown.

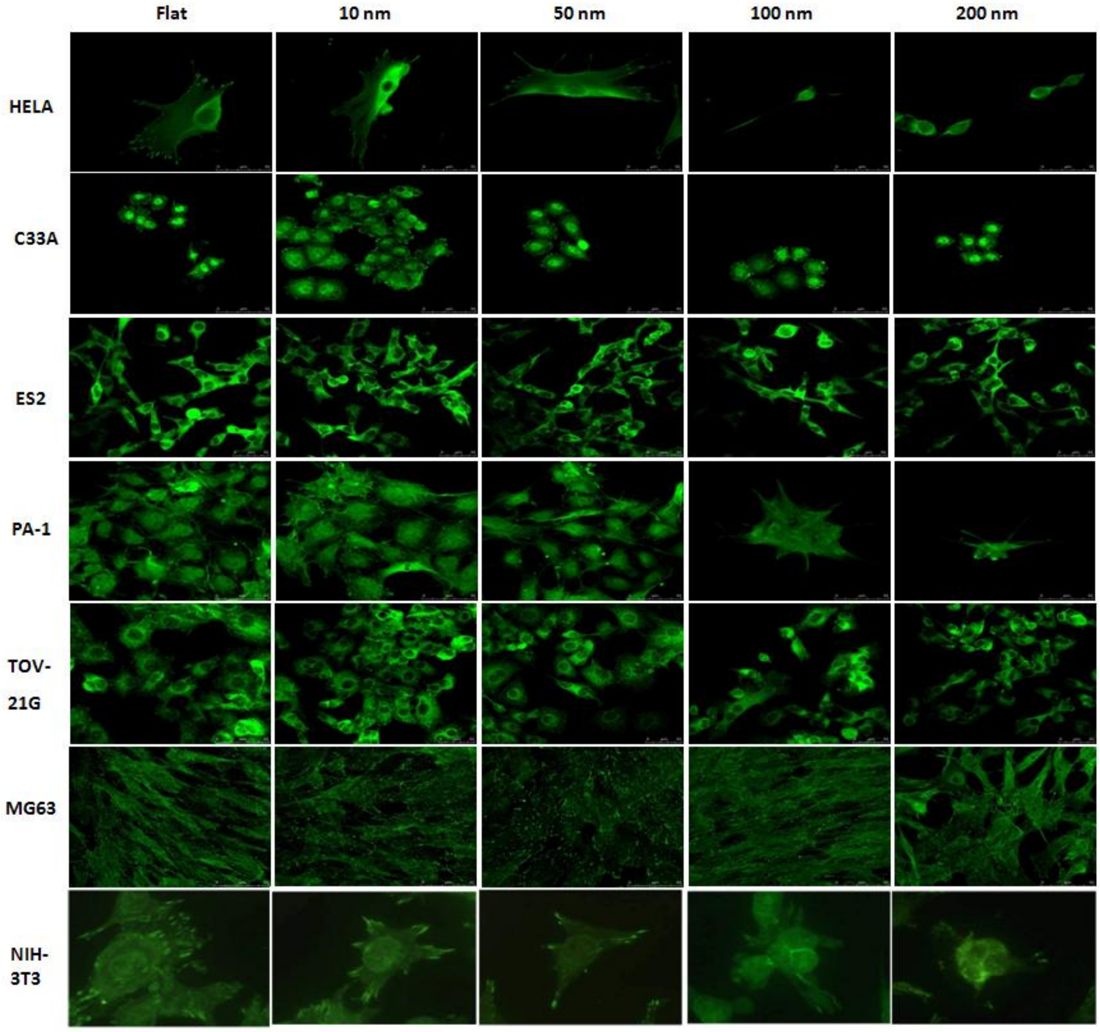

Figure 30 *Immunostaining for distribution of vinculin in cells cultured on 10 nm, 50 nm, 100 nm, and 200 nm nanodot arrays and on a flat surface. Cells were seeded on arrays for 72 hours before harvest. The sample was incubated with anti-vinculin antibody (properly diluted in 0.5% BSA), followed by incubation with Alexa Fluor 488 goat anti-mouse antibody.*

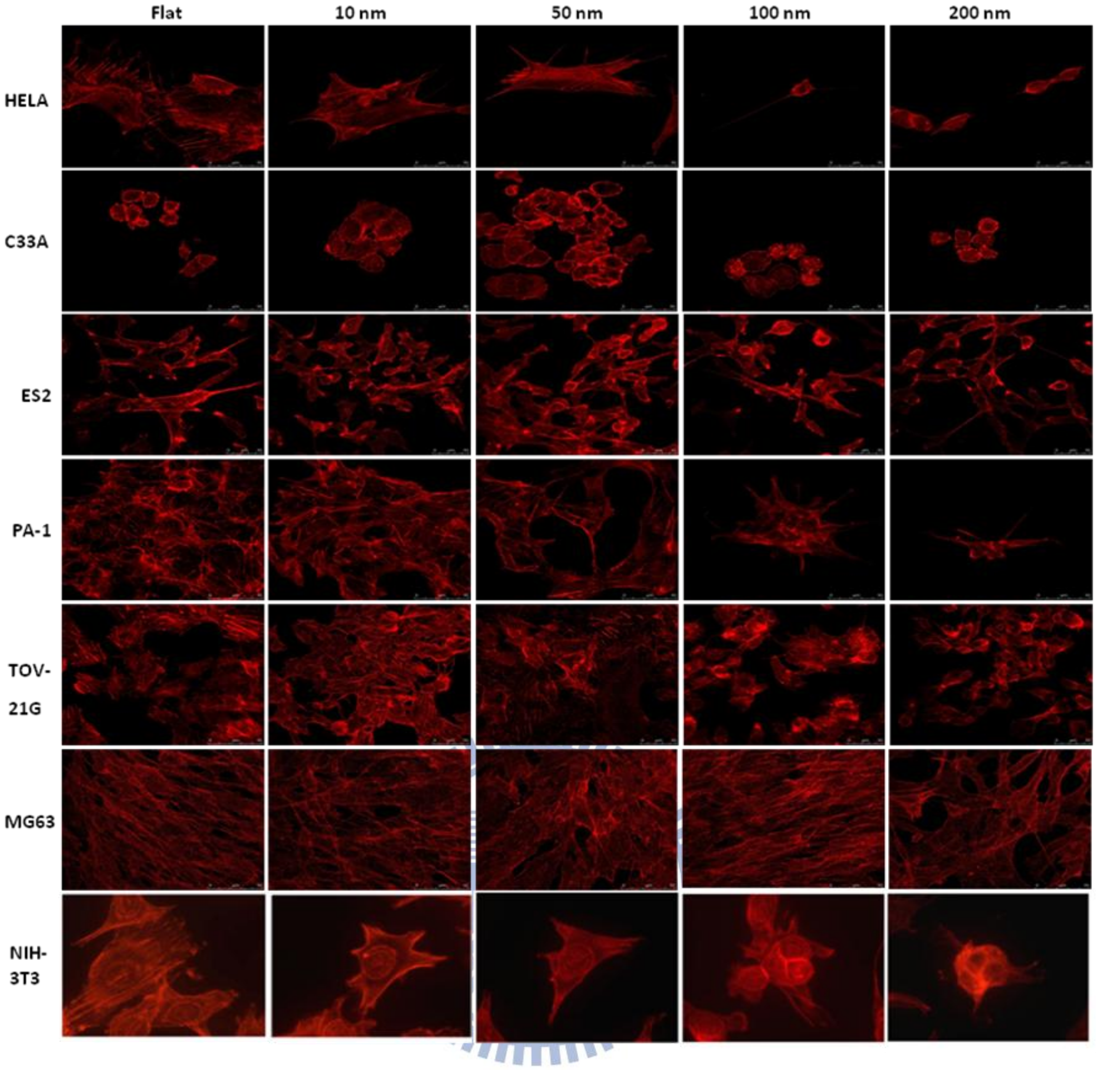

Figure 31 *Immunostaining for distribution of microfilaments in cells cultured on 10 nm, 50 nm, 100 nm, and 200 nm nanodot arrays and on a flat surface. Cells were seeded on arrays for 72 hours before harvest. The sample was incubated with phalloidin.*

To evaluate the size-dependent effects of nanodot arrays on cell growth, indices corresponding to cell proliferation, apoptosis, cell adhesion, and cytoskeletal organization were defined. VD_{50}, AD_{50}, FD_{50}, and CD_{50} scores for all cell lines employed in the current study. VD_{50} is defined as the diameter of nanodots on which 50% of the cell population remains viable compared to cells seeded on a flat surface after 3 days of incubation. VD_{50} for each cell line was derived by counting the number of cells on the nanodot arrays, drawing the graph of viability versus dot diameter, and calculating the dot diameter at which 50% viability was obtained (Figure 32).

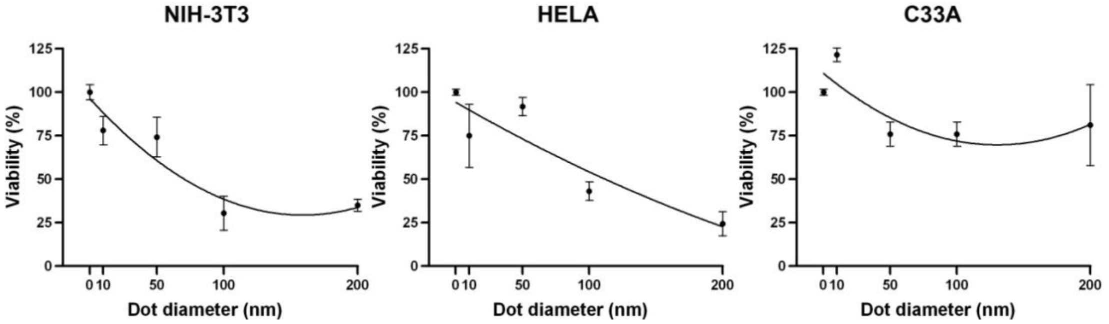

Figure 32 *Viability versus dot diameter for cells cultured on the nanodevice. Cells are cultured on the nanodevice for 3 days. The viable cells are counted and percent viability relative to cells cultured on a flat surface (0 nm) is calculated and graphed against the nanodot diameter. The graphs show viability of NIH-3T3 (left), HELA cells (center), and C33A (right). Each value is averaged from at least 6 independent experiments. The error bars are the standard errors. The curves for best fit are derived using SigmaPlot software.*

AD_{50} is defined as the diameter of nanodots on which 50% of the cell population appears to display apoptosis-like morphology after 3 days of incubation. AD_{50} was calculated by counting the percentage of apoptotic cells on the nanodots, drawing the graph of percent apoptotic cells versus dot diameter, and calculating the dot diameter that causes 50% apoptosis (Figure 33).

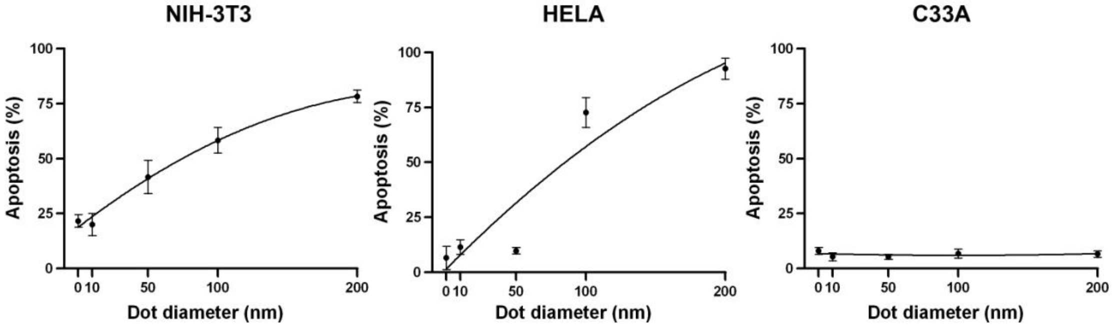

Figure 33 *Percent cells that have undergone apoptosis versus dot diameter for cells cultured on the nanodevice. Cells are cultured on the nanodevice for 3 days and SEM images are taken. Cells of apoptosis-like morphology are counted and percent apoptosis is calculated then graphed against the nanodot diameter. The graphs show percent apoptosis of NIH-3T3 (left), HELA cells (center), and C33A (right). Each value is averaged from at least 6 independent experiments. The error bars are the standard errors. The curves for best fit are derived using SigmaPlot software.*

FD_{50} is the diameter of nanodots that promotes the formation of 50% of the focal adhesions compared to cells grown on a flat surface. FD_{50} was calculated by counting the number of vinculin stained spots per cell, drawing the graph of percent focal adhesions versus dot diameter, and finding the diameter that promotes 50% of focal adhesions compared to a flat surface (Figure 34).

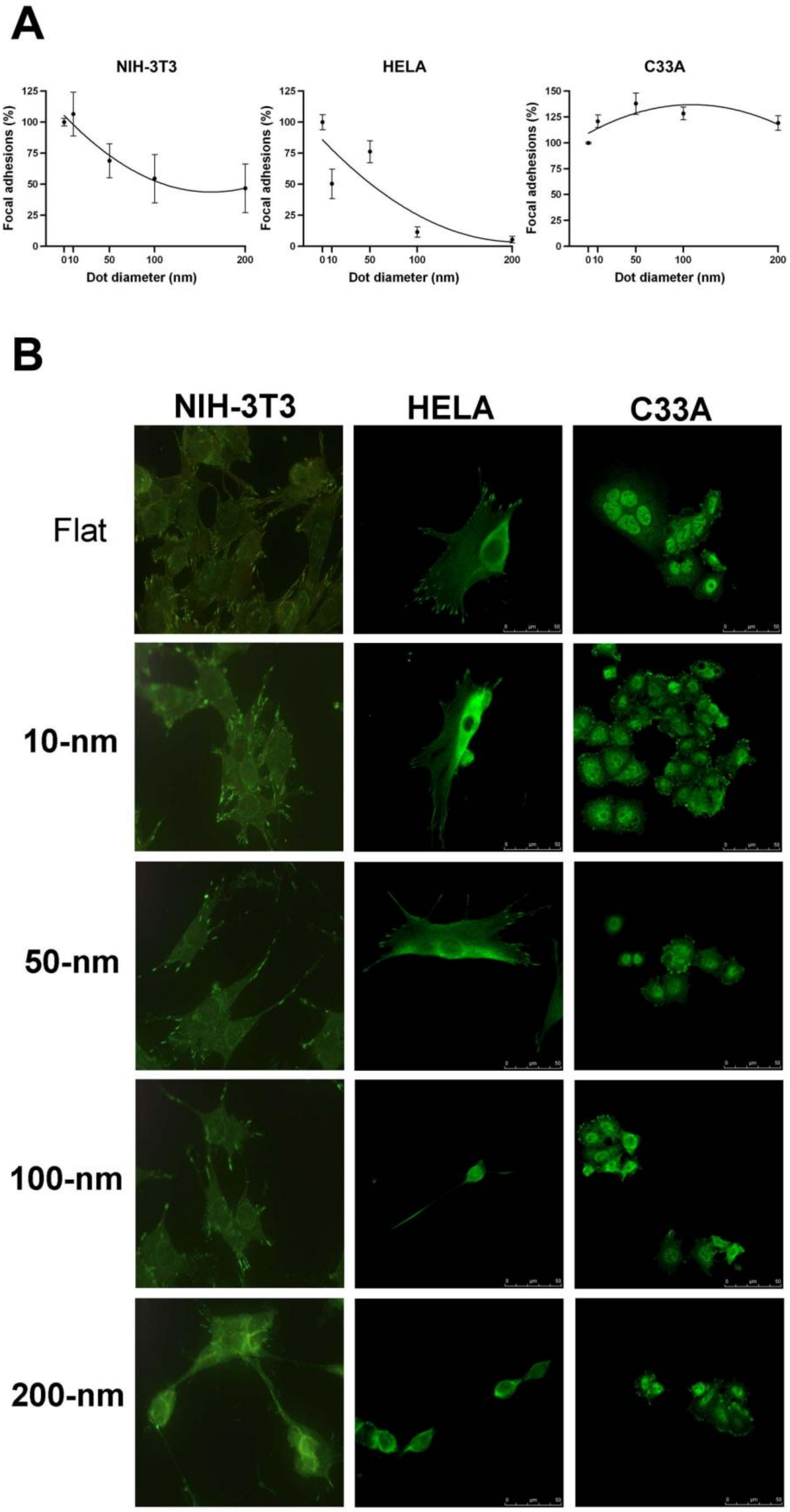

Figure 34 *Percent focal adhesions versus dot diameter for cells cultured on the nanodevice. Cells are cultured on the nanodevice for 3 days and immunostaining using*

anti-vinculin antibody is performed. Number of vinculin stains per cell is counted and percent focal adhesions relative to cells grown on a flat surface is calculated, then graphed against nanodot diameter (A). The graphs show percent focal adhesions of NIH-3T3 (left), HELA cells (center), and C33A (right). Each value is averaged from at least 6 independent experiments. The error bars are the standard errors. The curves for best fit are derived using SigmaPlot software. Representative images used in the measurement are shown (B).

CD_{50} is the diameter of nanodots on which cells exhibit half the number of microfilament bundles compared to cells grown on a flat surface. Microfilaments (or actin filaments) are the thinnest filaments of the cytoskeleton found in the cytoplasm of all eukaryotic cells. Actin filaments are assembled in two general types of structures: bundles and networks. These structures are regulated by many other classes of actin-binding proteins. With confocal microscopy, an estimation for the number of microfilament bundles can be obtained by building a 3-d cell image. CD_{50} was calculated by counting the number of microfilament bundles per cell, drawing the graph of microfilament bundles versus dot diameter, and obtaining the diameter that gives a two-fold reduction in the amount of microfilament bundles compared to cells grown on a flat surface (Figure 35).

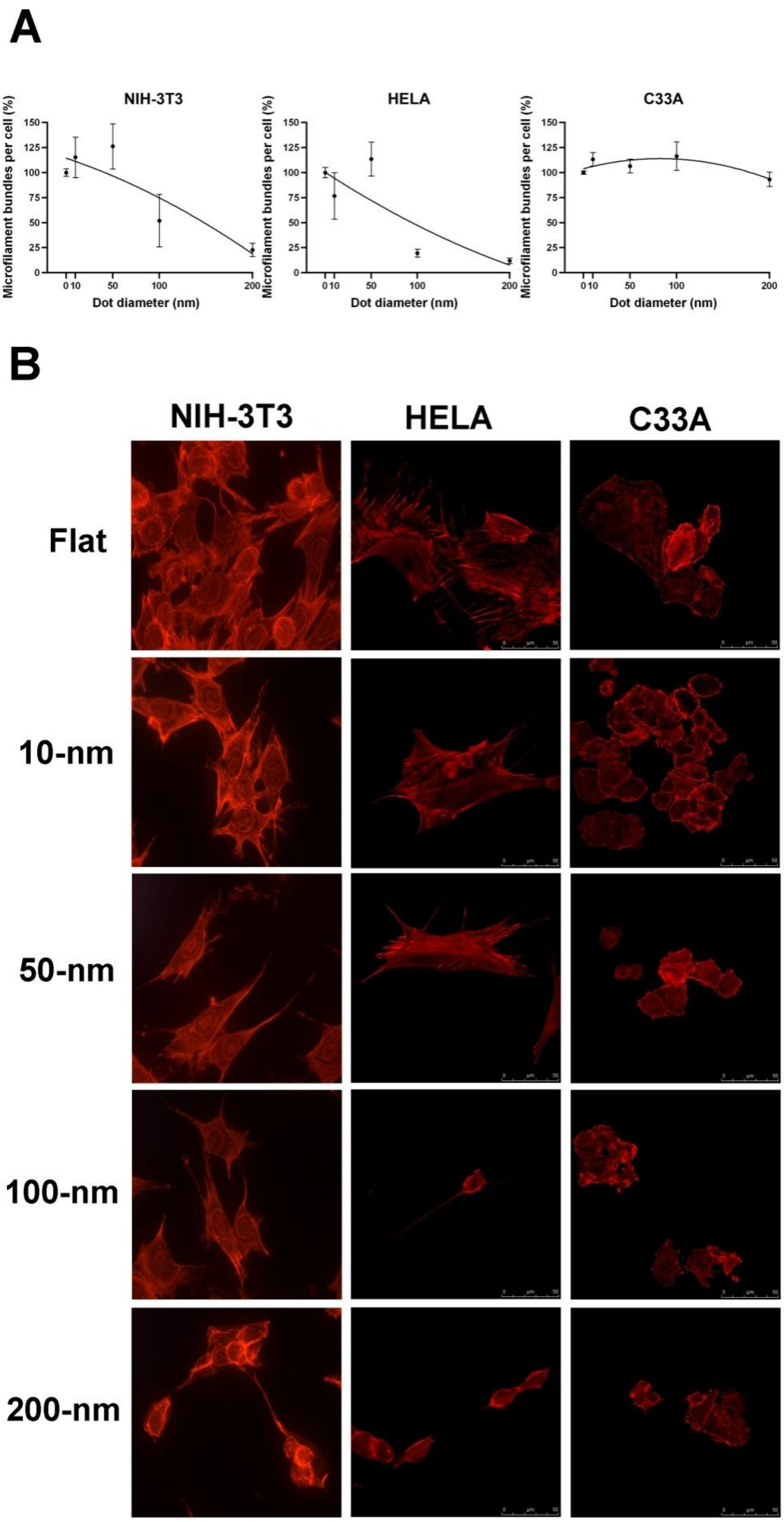

Figure 35 *Percent microfilament bundles per cell versus dot diameter for cells cultured on the nanodevice. Cells are cultured on the nanodevice for 3 days and phalloidin staining is performed. 3-d fluorescence images are obtained using a confocal*

microscope. The number of microfilament bundles per cell is counted and percent microfilament bundles relative to cells grown on a flat surface is calculated and graphed against nanodot diameter (A). The graphs show percent actin filaments of NIH-3T3 (left), HELA cells (center), and C33A (right). Each value is averaged from at least 6 independent experiments. The error bars are the standard errors. The curves for best fit are derived using SigmaPlot software. Representative images used in the measurement are shown (B).

NIH-3T3 cells, used as a normal control cell line in the current study, are a mouse embryonic fibroblast cell line established from a NIH Swiss mouse embryo. They are highly contact inhibited and are sensitive to sarcoma virus focus formation and leukemia virus propagation. This cell line was established from NIH Swiss mouse embryo cultures in the same manner as the original random-bred 3T3 and the inbred BALB/c 3T3. Viability was at 78% and 74.2% for 10 nm and 50 nm nanodots respectively, but dropped to 30.4% and 35% for 100 nm and 200 nm nanodot arrays respectively. VD_{50} for NIH-3T3 is 71 nm. The percentage of apoptosis-like cells was 58.3% for 100 nm and reached 78.3% for the 200 nm dot array. AD_{50} for NIH-3T3 is 75 nm. The vinculin staining indicated the density of focal adhesions, which dropped to 68.8% at 50 nm and decreased to 54.6% and 46.8% for 100 nm and 200 nm respectively. FD_{50} for NIH-3T3 is 110 nm. The cytoskeletal organization lost its order when the array size was larger than 100 nm. CD_{50} for NIH-3T3 is 148 nm (Table 6). The NIH-3T3 cell line grew well on flat, 10 nm, and 50 nm surfaces, but dropped to apoptotic levels and lost cell adhesion if the nanodot size was larger than 100 nm.

HELA cells are a human cervical cancer cell line carrying human papillomavirus-18 (HPV-18), with a low level of p53 expression. HELA cells are an immortal cell line used in scientific research. Viability was maintained at 91.7% for 50 nm, but it dropped to 43.2% when the nanodot size reached 100 nm, and further dropped to 24.4% for the 200 nm nanodot array. VD_{50} for HELA cells is 112 nm. The cell morphology remained flat and extended at 50 nm, but mounted and changed to an apoptosis-like shape for 100 nm and 200 nm surfaces. AD_{50} for HELA cells is 85 nm. Immunostaining indicated enhanced staining of vinculin, which represented enhanced cell adhesion for sizes under 50 nm. FD_{50} for HELA cells is 51 nm. The cytoskeletal organization lost its order when the size was larger than 100 nm. CD_{50} for HELA cells is 94 nm (Table 6). In summary, HELA cells grew well and reached optimized conditions at 50 nm, but lost cell adhesion and switched to an apoptotic mode when the dot size was larger than 100 nm. Compared to NIH-3T3 cells, HELA cells exhibited higher VD_{50} and AD_{50} but had lower FD_{50} and CD_{50}. Although HELA cells proliferated better than NIH-3T3 cells on the nanosurfaces, the cytoskeletal organization associated with the formation of focal adhesions appeared to be less tolerable to changes in nanosurfaces.

C33A cells represent a human cervical cancer cell line derived from advanced carcinoma with highly invasive activity and with negative expression for HPV DNA and RNA. No significant difference in proliferation was observed among all nanodot arrays, from flat to 200 nm. The cell morphology remained flat and extended at all sizes of the nanodot arrays. The immunostaining showed no significant difference in the number of focal adhesions. Cells grown at all conditions displayed well-organized cytoskeletons. All indices are higher than 200 nm (Table 6). Compared to HELA cells, C33A cells proliferated and developed well-organized focal adhesions and cytoskeletons on all sizes of nanosurface. This cell behavior might be an indication that C33A is derived from cervical cancer that is at a later stage than the cancer from which HELA cells were derived.

The ES-2 cell line was established from a surgical tumor specimen taken from a 47-year-old black woman. The tumor was described as a poorly differentiated ovarian clear cell carcinoma. This cell line exhibits low to moderate resistance to a number of chemotherapeutic agents including doxorubicin, cisplatin, carmustine, etoposide, and cyanomorpholinodoxorubicin (MRA-CN). It also expresses low levels of P glycoprotein. The viability for ES2 cells dropped to 61.3% for 100 nm and to 70.9% for 200 nm nanodots. The morphology was extended on surfaces ranging from a flat surface to 100 nm nanodots. The morphology indicated that apoptosis occurred when the nanodot size reached 200 nm. Immunostaining of vinculin showed that the number of focal adhesions decreased dramatically when cells were grown on a 200 nm dot array, and cytoskeletal organization became disordered at 200 nm. VD_{50}, AD_{50}, FD_{50}, and CD_{50} for ES2 are >200, 198, >200, and >200 nm, respectively (Table 6). In summary, ES2 cells grew well on a flat surface and on nanodots up to 100 nm, but showed apoptosis and loss of cell adhesion at 200 nm.

The human ovarian teratocarcinoma cell line PA-1 was isolated from the ascites fluid of a 12-year-old girl suffering from recurrent malignant teratocarcinoma. Malignant ovarian teratocarcinomas differ from their benign counterparts in that they are a rare form of tumor and usually occur in prepubertal females. They consist of many immature elements and can arise by several mechanisms, including failure of meiosis I or II or fusion of two ova. High passage PA-1 cells are tumorigenic in nude mice upon subcutaneous injection, form embryoid bodies under nonadherent culture conditions, and form colonies in soft agar. Cytogenetically, PA-1 has a stable diploid female karyotype with a single balanced translocation between chromosomes 15 and 20. Cell viability was enhanced and rose to 107.6% on surfaces with 50 nm nanodot arrays, but decreased to 30.2% when the nanodot size reached 100 nm, and further decreased to 12.6% at 200 nm. The morphology remained flat and extended until 50 nm, but mounted and began to exhibit apoptosis on surfaces with nanodots between 100 nm and 200 nm. Decreased staining of vinculin was observed, which indicated decreased cell adhesion for nanodot sizes larger than 100 nm. The cytoskeletal organization was less ordered when the dot size was greater than 100 nm. VD_{50}, AD_{50}, FD_{50}, and CD_{50} for PA-1 are 108, 147, 72, and 142 nm, respectively (Table 6). In summary, PA-1 cells grew well and reached optimized conditions on 50 nm arrays, but displayed apoptosis and loss of cell adhesion if the nanodot size was larger than 100 nm. PA-1 exhibited an earlier-staged cancerous behavior compared to the ES2 cell line.

TOV-112D cells represent a human ovarian cancer cell line derived from an endometrioid epithelial carcinoma from a 42-year-old female. It is a primary malignant adenocarcinoma of grade 3 and staged as IIIC. Viability did not change for cells grown on a flat surface to 50 nm nanodot arrays, but it decreased to 70% when the nanodot size reached 100 nm, and dropped to 50% at 200 nm. The morphology remained flat and extended at 50 nm, but mounted and showed apoptosis on 100 nm and 200 nm dot arrays. VD_{50}, AD_{50}, FD_{50}, and CD_{50} for TOV-112D are 198, 127, >200, and >200 nm, respectively (Table 6). In summary, TOV-112D cells grew well on flat, 10 nm, and 50 nm surfaces, but apoptosis occurred if the nanodot size was larger than 200 nm. TOV-112D exhibited characteristics of late-staged cancer.

TOV-21G cells are a human ovarian cancer cell line. These cells are from a clear cell epithelial carcinoma derived from a 62-year-old female. This is a primary malignant adenocarcinoma, of grade 3 and staged as III. Viability was enhanced and reached 110% when grown on 50 nm nanodot arrays, but decreased to 90% when the array size was 100 nm, and to 60% at 200 nm. The morphology remained flat and extended at 50 nm, but mounted and showed apoptosis on the 100 nm and 200 nm dot arrays. Immunostaining indicated slightly enhanced staining of vinculin for sizes under 50 nm. The cytoskeletal organization loses order when the size is larger than 100 nm. VD_{50}, AD_{50}, FD_{50}, and CD_{50} for TOV-21G are >200, >200, 68, and >200 nm, respectively (Table 6). In summary, TOV-21G cells grew well on flat, 10 nm, and 50 nm surfaces, but became apoptotic and showed loss of cell adhesion if the size was larger than 200 nm.

MG63 cells, a cell line derived from an osteosarcoma, produce high yields of interferon after superinduction with polyinosinic acid, polycytidylic acid, cycloheximide, and actinomycin D. Studies using MG63 cells provide some important mechanistic clues concerning the details of the amplification process in tumors. Viability was enhanced and reached 158% on 50 nm nanodot arrays, but dropped to 77.8% at 100 nm, and to 50% for the 200 nm nanodot array. The cell morphology became more flat and extended at 50 nm, but mounted and changed to an apoptotic shape on 100 nm and 200 nm dot array surfaces. Immunostaining showed enhanced staining of vinculin, which represents enhanced cell adhesion, for nanodot sizes under 50 nm. The cytoskeleton organization loses its order when the nanodot size is larger than 100 nm. VD_{50}, AD_{50}, FD_{50}, and CD_{50} for TOV-21G are 196, 143, >200, and >200 nm, respectively (Table 6). In summary, MG63 cells grew well and reached a maximized condition at 50 nm, but dropped back to normal levels if the size was larger than 100 nm.

Table 6 *VD_{50}, AD_{50}, FD_{50}, and CD_{50} of cell lines employed in the current study*

Cell line	**VD_{50}**^{a}(nm)	**VD_{75}** (nm)	**AD_{50}**^{b} (nm)	**FD_{50}**^{c} (nm)	**CD_{50}**^{d} (nm)	**CD_{75}** (nm)
HELA	112	35	85	51	94	45
C33A	>200	68	>200	>200	>200	>200
ES2	>200	167	198	>200	>200	167
PA-1	108	37	147	72	142	85
TOV-112D	198	110	127	>200	>200	>200
TOV-21G	>200	167	>200	68	>200	152
MG63	196	164	143	>200	>200	184
NIH-3T3	71	26	75	110	148	99

4. Conclusions

4.1 Nanodot array modulates cell adhesion and induces an apoptosis-like abnormality in 3T3 fibroblast

Our evidence supports the hypothesis that the formation of focal adhesions and the reorganization of the cytoskeleton are part of the apoptotic pathway triggered by nanotopography. The number of focal adhesions was decreased for cells cultured on the 50 nm arrays and was completely absent for cells on the 100 nm and 200 nm arrays. The organization of actin filaments was observed in cells cultured on flat surfaces and on the 10 nm nanodot arrays, but was absent in cells cultured on the 100 nm and 200 nm nanodot arrays. Pretreatment with FN and collagen forced cell adhesion and the formation of focal adhesions, which prevented the apoptosis-like abnormality of cells culturing on the 100 nm arrays. Since focal adhesions and the cytoskeleton play important roles in the nanotopology-induced apoptosis-like abnormality, it is likely that integrins are the receptors mediating the suicidal signal.

Nanotopography-induced apoptosis shares some common features with anoikis, the apoptosis induced by the loss of cell adhesion [121]. Both events were initiated at the bio-nano interface. The loss of focal adhesions and organization of actin filaments were key features of both phenomena. However, anoikis is triggered by forcing epithelial cells to grow in suspension, and signaling is detectable in minutes to hours [122]. Nanotopography-induced apoptosis-like events became evident only after days of incubation. We noticed that cells seemed to lose adhesion when grown on the 100 nm and 200 nm arrays (Figure 6). Serious deformation of cells was observed. The loss of attachment might be due to an imbalanced shear force caused by the uneven evaporation of solvent during the dehydration process. However, cells cultured on other nano-dot arrays maintained decent adhesion with the surface, indicating that the cells grown on the 100 nm and 200 nm arrays exhibited relatively weak binding affinity to the surface.

4.2 Topographic control of the growth and function of cardiomyoblast H9c2 cells using nanodot array

In this study, we showed that nanotopography can control the growth and function of cardiomyoblasts. Differential growth of cardiomyoblasts on nanodot arrays was demonstrated. The optimal growth, most extended morphology, largest surface area, and greatest proliferation occurred in cells cultured on 50 nm nanodot arrays. Implants fabricated using similar surfaces are anticipated to have better biocompatibility and be more suited to long-term function in the human body. The nanotopography of the 100- and 200 nm nanodot arrays reduced cell growth and attachment, thus inducing apoptosis in cells. qPCR showed that 50- and 100 nm nanodot arrays can induce fibrosis for H9c2 cardiomyoblasts. Nanodots of 100- and 200 nm in diameter could be incorporated into the surface of implants to purposely inhibit cell growth.

4.3 Optimization for the biocompatibility of dental implants using nano-structures/MG 63 osteoblasts model system

Here, we propose a strategy for the topologic design of dental implants based on an *in vitro* survey of optimized nanodot structures. The nanostructure is capable of modulating the *in vitro* growth and function of osteoblasts and is optimal with a nanodot size of approximately 50 nm in diameter. The clinical survey included four implants, two CaP-coated implants and two non-coated implants. The clinical results were consistent with the *in vitro* study. The best clinical outcome occurred with implants with nanostructures resembling the 50 nm nanodot array. Implant A contains approximately 20 nm nanocrystalline structures in a sparse and random distribution with dot-to-dot distance in a range that inhibits cell growth and function. Implant A behaves poorly in both the *in vitro* and clinical studies. The results indicated that the dot-to-dot distance may be a major concern for an isotropic surface.

4.4 A nanodevice for rapid modulation of proliferation, apoptosis, invasive ability, and cytoskeletal reorganization in cancer cells

We have established a platform that can be used to assess basic parameters for cell growth. The specific platform could be used to observe the proliferation, apoptosis, adhesion, and cytoskeletal organization of cells. The simplified fabrication process allows for mass production and lower costs. According to our results, the device is capable of distinguishing between cancer cell lines of various stages and also provides basic design parameters for artificial implants. Our device will serve as a convenient and fast tool for tissue engineering and cancer treatment.

5. References

[1] Abrams GA, Goodman SL, Nealey PF, Franco M, Murphy CJ. Nanoscale topography of the basement membrane underlying the corneal epithelium of the rhesus macaque. Cell Tissue Res. 2000;299:39-46.

[2] Teixeira AI, McKie GA, Foley JD, Bertics PJ, Nealey PF, Murphy CJ. The effect of environmental factors on the response of human corneal epithelial cells to nanoscale substrate topography. Biomaterials. 2006;27:3945-54.

[3] Ranucci CS, Moghe PV. Substrate microtopography can enhance cell adhesive and migratory responsiveness to matrix ligand density. J Biomed Mater Res. 2001;54:149-61.

[4] Karuri NW, Liliensiek S, Teixeira AI, Abrams G, Campbell S, Nealey PF, et al. Biological length scale topography enhances cell-substratum adhesion of human corneal epithelial cells. J Cell Sci. 2004;117:3153-64.

[5] Liliensiek SJ, Campbell S, Nealey PF, Murphy CJ. The scale of substratum topographic features modulates proliferation of corneal epithelial cells and corneal fibroblasts. J Biomed Mater Res A. 2006;79:185-92.

[6] Rowland TJ, Miller LM, Blaschke AJ, Doss EL, Bonham AJ, Hikita ST, et al. Roles of integrins in human induced pluripotent stem cell growth on Matrigel and vitronectin. Stem Cells Dev. 2010;19:1231-40.

[7] Kaiser JP, Reinmann A, Bruinink A. The effect of topographic characteristics on cell migration velocity. Biomaterials. 2006;27:5230-41.

[8] Kim DH, Seo CH, Han K, Kwon KW, Levchenko A, Suh KY. Guided Cell Migration on Microtextured Substrates with Variable Local Density and Anisotropy. Adv Funct Mater. 2009;19:1579-86.

[9] Petrie RJ, Doyle AD, Yamada KM. Random versus directionally persistent cell migration. Nat Rev Mol Cell Biol. 2009;10:538-49.

[10] Chang HY, Chi JT, Dudoit S, Bondre C, van de Rijn M, Botstein D, et al. Diversity, topographic differentiation, and positional memory in human fibroblasts. Proc Natl Acad Sci U S A. 2002;99:12877-82.

[11] Flemming RG, Murphy CJ, Abrams GA, Goodman SL, Nealey PF. Effects of synthetic micro- and nano-structured surfaces on cell behavior. Biomaterials. 1999;20:573-88.

[12] Mendonca G, Mendonca DB, Aragao FJ, Cooper LF. Advancing dental implant surface technology--from micron- to nanotopography. Biomaterials. 2008;29:3822-35.

[13] Brody S, Anilkumar T, Liliensiek S, Last JA, Murphy CJ, Pandit A. Characterizing nanoscale topography of the aortic heart valve basement

membrane for tissue engineering heart valve scaffold design. Tissue Eng. 2006;12:413-21.

[14] Hansen JC, Yul Lim J, Xu LC, Siedlecki CA, Mauger DT, Donahue HJ. Effect of surface nanoscale topography on elastic modulus of individual osteoblastic cells as determined by atomic force microscopy. Journal of biomechanics. 2007;40:2865-71.

[15] Palin E, Liu H, Webster TJ. Mimicking the nanofeatures of bone increases bone-forming cell adhesion and proliferation. Nanotechnology. 2005;16:1828.

[16] Lim JY, Dreiss AD, Zhou Z, Hansen JC, Siedlecki CA, Hengstebeck RW, et al. The regulation of integrin-mediated osteoblast focal adhesion and focal adhesion kinase expression by nanoscale topography. Biomaterials. 2007;28:1787-97.

[17] Lim JY, Hansen JC, Siedlecki CA, Runt J, Donahue HJ. Human foetal osteoblastic cell response to polymer-demixed nanotopographic interfaces. J R Soc Interface. 2005;2:97-108.

[18] Stevens MM, George JH. Exploring and engineering the cell surface interface. Science. 2005;310:1135-8.

[19] Miller DC, Haberstroh KM, Webster TJ. Mechanism (s) of increased vascular cell adhesion on nanostructured poly (lactic co glycolic acid) films. J Biomed Mater Res A. 2005;73:476-84.

[20] Miller DC, Thapa A, Haberstroh KM, Webster TJ. Endothelial and vascular smooth muscle cell function on poly (lactic-co-glycolic acid) with nano-structured surface features. Biomaterials. 2004;25:53-61.

[21] Yang Y, Leong KW. Nanoscale surfacing for regenerative medicine. Wiley Interdiscip Rev Nanomed Nanobiotechnol. 2010;2:478-95.

[22] Tanaka K, Ashizawa N, Kawano H, Sato O, Seto S, Nishihara E, et al. Aldosterone induces circadian gene expression of clock genes in H9c2 cardiomyoblasts. Heart Vessels. 2007;22:254-60.

[23] Pan HA, Hung YC, Sui YP, Huang GS. Topographic control of the growth and function of cardiomyoblast H9c2 cells using nanodot arrays. Biomaterials. 2012;33:20-8.

[24] Park JK, Kim YJ, Yeom J, Jeon JH, Yi GC, Je JH, et al. The topographic effect of zinc oxide nanoflowers on osteoblast growth and osseointegration. Adv Mater. 2010;22:4857-61.

[25] Zaveri TD, Dolgova NV, Chu BH, Lee J, Wong J, Lele TP, et al. Contributions of surface topography and cytotoxicity to the macrophage response to zinc oxide nanorods. Biomaterials. 2010;31:2999-3007.

[26] Zhao L, Hu L, Huo K, Zhang Y, Wu Z, Chu PK. Mechanism of cell repellence on quasi-aligned nanowire arrays on Ti alloy. Biomaterials. 2010;31:8341-9.

[27] Choi CH, Hagvall SH, Wu BM, Dunn JCY, Beygui RE, “Cj” Kim CJ. Cell interaction with three-dimensional sharp-tip nanotopography. Biomaterials. 2007;28:1672-9.

[28] Dalby MJ, McCloy D, Robertson M, Agheli H, Sutherland D, Affrossman S, et al. Osteoprogenitor response to semi-ordered and random nanotopographies. Biomaterials. 2006;27:2980-7.

[29] Wan Y, Wang Y, Liu Z, Qu X, Han B, Bei J, et al. Adhesion and proliferation of OCT-1 osteoblast-like cells on micro- and nano-scale topography structured poly(L-lactide). Biomaterials. 2005;26:4453-9.

[30] Rebollar E, Frischauf I, Olbrich M, Peterbauer T, Hering S, Preiner J, et al. Proliferation of aligned mammalian cells on laser-nanostructured polystyrene. Biomaterials. 2008;29:1796-806.

[31] Peng L, Eltgroth ML, LaTempa TJ, Grimes CA, Desai TA. The effect of TiO2 nanotubes on endothelial function and smooth muscle proliferation. Biomaterials. 2009;30:1268-72.

[32] Dalby MJ, Riehle MO, Sutherland DS, Agheli H, Curtis AS. Changes in fibroblast morphology in response to nano-columns produced by colloidal lithography. Biomaterials. 2004;25:5415-22.

[33] Dolatshahi-Pirouz A, Pennisi CP, Skeldal S, Foss M, Chevallier J, Zachar V, et al. The influence of glancing angle deposited nano-rough platinum surfaces on the adsorption of fibrinogen and the proliferation of primary human fibroblasts. Nanotechnology. 2009;20:095101.

[34] Lovmand J, Justesen J, Foss M, Lauridsen RH, Lovmand M, Modin C, et al. The use of combinatorial topographical libraries for the screening of enhanced osteogenic expression and mineralization. Biomaterials. 2009;30:2015-22.

[35] Dalby MJ, Gadegaard N, Tare R, Andar A, Riehle MO, Herzyk P, et al. The control of human mesenchymal cell differentiation using nanoscale symmetry and disorder. Nat Mater. 2007;6:997-1003.

[36] Dalby MJ, Riehle MO, Johnstone HJ, Affrossman S, Curtis AS. Polymer-demixed nanotopography: control of fibroblast spreading and proliferation. Tissue Eng. 2002;8:1099-108.

[37] Park J, Bauer S, Schlegel KA, Neukam FW, von der Mark K, Schmuki P. TiO2 nanotube surfaces: 15 nm--an optimal length scale of surface topography for cell adhesion and differentiation. Small. 2009;5:666-71.

[38] Biggs MJP, Richards RG, Gadegaard N, Wilkinson CDW, Dalby MJ. The effects of nanoscale pits on primary human osteoblast adhesion formation and cellular spreading. Journal of Materials Science: Materials in Medicine. 2007;18:399-404.

[39] Hart A, Gadegaard N, Wilkinson CD, Oreffo RO, Dalby MJ. Osteoprogenitor response to low-adhesion nanotopographies originally fabricated by electron beam lithography. J Mater Sci Mater Med. 2007;18:1211-8.

[40] Liliensiek SJ, Wood JA, Yong J, Auerbach R, Nealey PF, Murphy CJ. Modulation of human vascular endothelial cell behaviors by nanotopographic cues. Biomaterials. 2010;31:5418-26.

[41] Xie J, Macewan MR, Ray WZ, Liu W, Siewe DY, Xia Y. Radially aligned, electrospun nanofibers as dural substitutes for wound closure and tissue regeneration applications. ACS Nano. 2010;4:5027-36.

[42] Park YS, Yi KY, Lee IS, Han CH, Jung YC. The effects of ion beam-assisted deposition of hydroxyapatite on the grit-blasted surface of endosseous implants in rabbit tibiae. Int J Oral Maxillofac Implants. 2005;20:31-8.

[43] Klabunde KJ, Stark J, Koper O, Mohs C, Park DG, Decker S, et al. Nanocrystals as stoichiometric reagents with unique surface chemistry. The Journal of Physical Chemistry. 1996;100:12142-53.

[44] Baraton MI, Chen X, Gonsalves K. FTIR study of a nanostructured aluminum nitride powder surface: Determination of the acidic/basic sites by CO, CO2 and acetic acid adsorptions. Nanostructured materials. 1997;8:435-45.

[45] Wu SJ, Jonghe LC, Rahaman MN. Sintering of Nanophase γ-Al2O3 Powder. Journal of the American Ceramic Society. 1996;79:2207-11.

[46] Zhao G, Zinger O, Schwartz Z, Wieland M, Landolt D, Boyan BD. Osteoblast-like cells are sensitive to submicron-scale surface structure. Clin Oral Implants Res. 2006;17:258-64.

[47] Cooper LF, Masuda T, Whitson SW, Yliheikkila P, Felton DA. Formation of mineralizing osteoblast cultures on machined, titanium oxide grit-blasted, and plasma-sprayed titanium surfaces. Int J Oral Maxillofac Implants. 1999;14:37-47.

[48] Mustafa K, Wroblewski J, Hultenby K, Lopez BS, Arvidson K. Effects of titanium surfaces blasted with TiO2 particles on the initial attachment of cells derived from human mandibular bone. A scanning electron microscopic and histomorphometric analysis. Clin Oral Implants Res. 2000;11:116-28.

[49] Webster TJ, Schadler LS, Siegel RW, Bizios R. Mechanisms of enhanced osteoblast adhesion on nanophase alumina involve vitronectin. Tissue Eng. 2001;7:291-301.

[50] Elias KL, Price RL, Webster TJ. Enhanced functions of osteoblasts on nanometer diameter carbon fibers. Biomaterials. 2002;23:3279-87.

[51] Price RL, Ellison K, Haberstroh KM, Webster TJ. Nanometer surface roughness increases select osteoblast adhesion on carbon nanofiber compacts. Journal of

Biomedical Materials Research. 2004;70:129-38.

[52] Alsberg E, Feinstein E, Joy MP, Prentiss M, Ingber DE. Magnetically-guided self-assembly of fibrin matrices with ordered nano-scale structure for tissue engineering. Tissue Eng. 2006;12:3247-56.

[53] McManus AJ, Doremus RH, Siegel RW, Bizios R. Evaluation of cytocompatibility and bending modulus of nanoceramic/polymer composites. J Biomed Mater Res A. 2005;72:98-106.

[54] Dalby MJ, Riehle MO, Johnstone H, Affrossman S, Curtis AS. In vitro reaction of endothelial cells to polymer demixed nanotopography. Biomaterials. 2002;23:2945-54.

[55] Nur EKA, Ahmed I, Kamal J, Schindler M, Meiners S. Three dimensional nanofibrillar surfaces induce activation of Rac. Biochem Biophys Res Commun. 2005;331:428-34.

[56] Park J, Bauer S, von der Mark K, Schmuki P. Nanosize and vitality: TiO2 nanotube diameter directs cell fate. Nano Lett. 2007;7:1686-91.

[57] Partridge MA, Marcantonio EE. Initiation of attachment and generation of mature focal adhesions by integrin-containing filopodia in cell spreading. Mol Biol Cell. 2006;17:4237-48.

[58] Choudhary S, Haberstroh KM, Webster TJ. Enhanced functions of vascular cells on nanostructured Ti for improved stent applications. Tissue Eng. 2007;13:1421-30.

[59] Robertson SW, Imbeni V, Wenk HR, Ritchie RO. Crystallographic texture for tube and plate of the superelastic/shape-memory alloy Nitinol used for endovascular stents. J Biomed Mater Res A. 2005;72:190-9.

[60] Verheye S, Markou CP, Salame MY, Wan B, King SB, 3rd, Robinson KA, et al. Reduced thrombus formation by hyaluronic acid coating of endovascular devices. Arterioscler Thromb Vasc Biol. 2000;20:1168-72.

[61] Chen JY, Leng YX, Tian XB, Wang LP, Huang N, Chu PK, et al. Antithrombogenic investigation of surface energy and optical bandgap and hemocompatibility mechanism of Ti(Ta(+5))O2 thin films. Biomaterials. 2002;23:2545-52.

[62] Dolmatch B, Dong YH, Heeter Z. Evaluation of three polytetrafluoroethylene stent-grafts in a model of neointimal hyperplasia. J Vasc Interv Radiol. 2007;18:527-34.

[63] Schuler P, Assefa D, Ylanne J, Basler N, Olschewski M, Ahrens I, et al. Adhesion of monocytes to medical steel as used for vascular stents is mediated by the integrin receptor Mac-1 (CD11b/CD18; alphaM beta2) and can be inhibited by semiconductor coating. Cell Commun Adhes. 2003;10:17-26.

[64] Achneck HE, Jamiolkowski RM, Jantzen AE, Haseltine JM, Lane WO, Huang JK, et al. The biocompatibility of titanium cardiovascular devices seeded with autologous blood-derived endothelial progenitor cells: EPC-seeded antithrombotic Ti implants. Biomaterials. 2011;32:10-8.

[65] Hehrlein C, Zimmermann M, Metz J, Ensinger W, Kubler W. Influence of surface texture and charge on the biocompatibility of endovascular stents. Coron Artery Dis. 1995;6:581-6.

[66] Cremonesi A, Benit E, Carlier M, Colombo A, Piva R, Probst P, et al. Multicenter registry to evaluate the efficacy of the NIROYAL stent in de novo or restenotic coronary stenosis. J Invasive Cardiol. 2000;12:225-32.

[67] Hoffmann R, Mintz GS, Haager PK, Bozoglu T, Grube E, Gross M, et al. Relation of stent design and stent surface material to subsequent in-stent intimal hyperplasia in coronary arteries determined by intravascular ultrasound. Am J Cardiol. 2002;89:1360-4.

[68] Heublein B, Ozbek C, Pethig K. Silicon carbide-coated stents: clinical experience in coronary lesions with increased thrombotic risk. J Endovasc Surg. 1998;5:32-6.

[69] Babapulle MN, Eisenberg MJ. Coated stents for the prevention of restenosis: Part II. Circulation. 2002;106:2859-66.

[70] Caves JM, Chaikof EL. The evolving impact of microfabrication and nanotechnology on stent design. J Vasc Surg. 2006;44:1363-8.

[71] Doyle B, Rihal CS, O'Sullivan CJ, Lennon RJ, Wiste HJ, Bell M, et al. Outcomes of stent thrombosis and restenosis during extended follow-up of patients treated with bare-metal coronary stents. Circulation. 2007;116:2391-8.

[72] Wall I, Donos N, Carlqvist K, Jones F, Brett P. Modified titanium surfaces promote accelerated osteogenic differentiation of mesenchymal stromal cells in vitro. Bone. 2009;45:17-26.

[73] Borsari V, Giavaresi G, Fini M, Torricelli P, Tschon M, Chiesa R, et al. Comparative in vitro study on a ultra-high roughness and dense titanium coating. Biomaterials. 2005;26:4948-55.

[74] Borsari V, Giavaresi G, Fini M, Torricelli P, Salito A, Chiesa R, et al. Physical characterization of different-roughness titanium surfaces, with and without hydroxyapatite coating, and their effect on human osteoblast-like cells. J Biomed Mater Res B Appl Biomater. 2005;75:359-68.

[75] Le Guehennec L, Lopez-Heredia MA, Enkel B, Weiss P, Amouriq Y, Layrolle P. Osteoblastic cell behaviour on different titanium implant surfaces. Acta Biomater. 2008;4:535-43.

[76] Schwartz Z, Olivares-Navarrete R, Wieland M, Cochran DL, Boyan BD.

Mechanisms regulating increased production of osteoprotegerin by osteoblasts cultured on microstructured titanium surfaces. Biomaterials. 2009;30:3390-6.

[77] Jager M, Zilkens C, Zanger K, Krauspe R. Significance of nano- and microtopography for cell-surface interactions in orthopaedic implants. J Biomed Biotechnol. 2007;2007:69036.

[78] Francois P, Vaudaux P, Taborelli M, Tonetti M, Lew DP, Descouts P. Influence of surface treatments developed for oral implants on the physical and biological properties of titanium. (II) Adsorption isotherms and biological activity of immobilized fibronectin. Clin Oral Implants Res. 1997;8:217-25.

[79] Taborelli M, Jobin M, Francois P, Vaudaux P, Tonetti M, Szmukler-Moncler S, et al. Influence of surface treatments developed for oral implants on the physical and biological properties of titanium. (I) Surface characterization. Clin Oral Implants Res. 1997;8:208-16.

[80] Silva TS, Machado DC, Viezzer C, Silva Junior AN, Oliveira MG. Effect of titanium surface roughness on human bone marrow cell proliferation and differentiation: an experimental study. Acta Cir Bras. 2009;24:200-5.

[81] Khang D, Lu J, Yao C, Haberstroh KM, Webster TJ. The role of nanometer and sub-micron surface features on vascular and bone cell adhesion on titanium. Biomaterials. 2008;29:970-83.

[82] Munoz-Casado MJ, Romance AI, Garcia-Recuero JI. Bioabsorbable osteofixation devices in craniosynostosis. Clinical experience in 216 cases. Neurocirugia (Astur). 2009;20:255-61.

[83] Toljanic JA, Baer RA, Ekstrand K, Thor A. Implant rehabilitation of the atrophic edentulous maxilla including immediate fixed provisional restoration without the use of bone grafting: a review of 1-year outcome data from a long-term prospective clinical trial. Int J Oral Maxillofac Implants. 2009;24:518-26.

[84] Lohmann CH, Sagun R, Jr., Sylvia VL, Cochran DL, Dean DD, Boyan BD, et al. Surface roughness modulates the response of MG63 osteoblast-like cells to 1,25-(OH)(2)D(3) through regulation of phospholipase A(2) activity and activation of protein kinase A. J Biomed Mater Res. 1999;47:139-51.

[85] Boyan BD, Sylvia VL, Liu Y, Sagun R, Cochran DL, Lohmann CH, et al. Surface roughness mediates its effects on osteoblasts via protein kinase A and phospholipase A2. Biomaterials. 1999;20:2305-10.

[86] Chehroudi B, McDonnell D, Brunette DM. The effects of micromachined surfaces on formation of bonelike tissue on subcutaneous implants as assessed by radiography and computer image processing. J Biomed Mater Res. 1997;34:279-90.

[87] Matsuo M, Nakamura T, Kishi Y, Takahashi K. Microvascular changes after

placement of titanium implants: scanning electron microscopy observations of machined and titanium plasma-sprayed implants in dogs. J Periodontol. 1999;70:1330-8.

[88] Ong JL, Carnes DL, Cardenas HL, Cavin R. Surface roughness of titanium on bone morphogenetic protein-2 treated osteoblast cells in vitro. Implant Dent. 1997;6:19-24.

[89] Ward BC, Webster TJ. The effect of nanotopography on calcium and phosphorus deposition on metallic materials in vitro. Biomaterials. 2006;27:3064-74.

[90] Zhu B, Lu Q, Yin J, Hu J, Wang Z. Alignment of osteoblast-like cells and cell-produced collagen matrix induced by nanogrooves. Tissue Eng. 2005;11:825-34.

[91] Bacac M, Stamenkovic I. Metastatic cancer cell. Annu Rev Pathol. 2008;3:221-47.

[92] Friedl P, Wolf K. Tumour-cell invasion and migration: diversity and escape mechanisms. Nat Rev Cancer. 2003;3:362-74.

[93] Reuning U, Magdolen V, Wilhelm O, Fischer K, Lutz V, Graeff H, et al. Multifunctional potential of the plasminogen activation system in tumor invasion and metastasis (review). Int J Oncol. 1998;13:893-906.

[94] Shen MR, Chou CY, Ellory JC. Volume-sensitive KCI cotransport associated with human cervical carcinogenesis. Pflugers Arch. 2000;440:751-60.

[95] Wu CT, Ko FH, Hwang HY. Self-aligned tantalum oxide nanodot arrays through anodic alumina template. Microelectronic Engineering. 2006;83:1567-70.

[96] Kriparamanan R, Aswath P, Zhou A, Tang L, Nguyen KT. Nanotopography: cellular responses to nanostructured materials. J Nanosci Nanotechnol. 2006;6:1905-19.

[97] Zaouk R, Park BY, Madou MJ. Fabrication of polydimethylsiloxane microfluidics using SU-8 molds. Methods Mol Biol. 2006;321:17-21.

[98] Cetrullo S, Facchini A, Stanic I, Tantini B, Pignatti C, Caldarera CM, et al. Difluoromethylornithine inhibits hypertrophic, pro-fibrotic and pro-apoptotic actions of aldosterone in cardiac cells. Amino Acids. 2010;38:525-31.

[99] Sueur S, Pesant M, Rochette L, Connat JL. Antiapoptotic effect of calcitonin gene-related peptide on oxidative stress-induced injury in H9c2 cardiomyocytes via the RAMP1/CRLR complex. J Mol Cell Cardiol. 2005;39:955-63.

[100] Wang H, Lin G, Zhang Z. ATF5 promotes cell survival through transcriptional activation of Hsp27 in H9c2 cells. Cell Biol Int. 2007;31:1309-15.

[101] Wolf NS, Penn PE, Rao D, McKee MD. Intraclonal plasticity for bone, smooth muscle, and adipocyte lineages in bone marrow stroma fibroblastoid cells. Exp Cell Res. 2003;290:346-57.

[102] Jager M, Feser T, Denck H, Krauspe R. Proliferation and osteogenic differentiation of mesenchymal stem cells cultured onto three different polymers in vitro. Ann Biomed Eng. 2005;33:1319-32.

[103] Koch TG, Heerkens T, Thomsen PD, Betts DH. Isolation of mesenchymal stem cells from equine umbilical cord blood. BMC Biotechnol. 2007;7:26.

[104] Venugopal J, Low S, Choon AT, Kumar AB, Ramakrishna S. Electrospun-modified nanofibrous scaffolds for the mineralization of osteoblast cells. J Biomed Mater Res A. 2008;85:408-17.

[105] Clark EA, Brugge JS. Integrins and signal transduction pathways: the road taken. Science. 1995;268:233-9.

[106] Hynes RO. Integrins: versatility, modulation, and signaling in cell adhesion. Cell. 1992;69:11-25.

[107] Dalby MJ, Childs S, Riehle MO, Johnstone HJ, Affrossman S, Curtis AS. Fibroblast reaction to island topography: changes in cytoskeleton and morphology with time. Biomaterials. 2003;24:927-35.

[108] Dalby MJ, Giannaras D, Riehle MO, Gadegaard N, Affrossman S, Curtis AS. Rapid fibroblast adhesion to 27nm high polymer demixed nano-topography. Biomaterials. 2004;25:77-83.

[109] Andersson AS, Backhed F, von Euler A, Richter-Dahlfors A, Sutherland D, Kasemo B. Nanoscale features influence epithelial cell morphology and cytokine production. Biomaterials. 2003;24:3427-36.

[110] Harris MB, Ju H, Venema VJ, Blackstone M, Venema RC. Role of heat shock protein 90 in bradykinin-stimulated endothelial nitric oxide release. Gen Pharmacol. 2000;35:165-70.

[111] Ilangovan G, Osinbowale S, Bratasz A, Bonar M, Cardounel AJ, Zweier JL, et al. Heat shock regulates the respiration of cardiac H9c2 cells through upregulation of nitric oxide synthase. Am J Physiol Cell Physiol. 2004;287:C1472-81.

[112] Fukai N, Shichiri M, Ozawa N, Matsushita M, Hirata Y. Coexpression of calcitonin receptor-like receptor and receptor activity-modifying protein 2 or 3 mediates the antimigratory effect of adrenomedullin. Endocrinology. 2003;144:447-53.

[113] Ichikawa-Shindo Y, Sakurai T, Kamiyoshi A, Kawate H, Iinuma N, Yoshizawa T, et al. The GPCR modulator protein RAMP2 is essential for angiogenesis and vascular integrity. J Clin Invest. 2008;118:29-39.

[114] Hou Q, Hsu YT. Bax translocates from cytosol to mitochondria in cardiac cells during apoptosis: development of a GFP-Bax-stable H9c2 cell line for apoptosis analysis. Am J Physiol Heart Circ Physiol. 2005;289:H477-87.

[115] Mayorga M, Bahi N, Ballester M, Comella JX, Sanchis D. Bcl-2 is a key factor for cardiac fibroblast resistance to programmed cell death. J Biol Chem. 2004;279:34882-9.

[116] Kutschka I, Kofidis T, Chen IY, von Degenfeld G, Zwierzchoniewska M, Hoyt G, et al. Adenoviral human BCL-2 transgene expression attenuates early donor cell death after cardiomyoblast transplantation into ischemic rat hearts. Circulation. 2006;114:I-174.

[117] Sharpe JC, Arnoult D, Youle RJ. Control of mitochondrial permeability by Bcl-2 family members. Biochim Biophys Acta. 2004;1644:107-13.

[118] Watkins SJ, Borthwick GM, Arthur HM. The H9C2 cell line and primary neonatal cardiomyocyte cells show similar hypertrophic responses in vitro. In Vitro Cell Dev Biol Anim. 2010;47:125-31.

[119] Laverriere AC, MacNeill C, Mueller C, Poelmann RE, Burch JB, Evans T. GATA-4/5/6, a subfamily of three transcription factors transcribed in developing heart and gut. J Biol Chem. 1994;269:23177-84.

[120] Xu W, Baribault H, Adamson ED. Vinculin knockout results in heart and brain defects during embryonic development. Development. 1998;125:327-37.

[121] Valentijn AJ, Zouq N, Gilmore AP. Anoikis. Biochem Soc Trans. 2004;32:421-5.

[122] Grossmann J, Walther K, Artinger M, Kiessling S, Scholmerich J. Apoptotic signaling during initiation of detachment-induced apoptosis ("anoikis") of primary human intestinal epithelial cells. Cell Growth Differ. 2001;12:147-55.

LIST OF PUBLICATIONS

Journal publication:

1. Pan HA, Liang JY, Hung YC, Chiou JC, Onsischuk AA, Huang GS. Nanotopographical sensing and adaptation of cell migration through temporal regulation of integrins in fibroblasts. *Eur Cells Mater.* 2012 (IF: 9.65) revised

2. Pan HA, Hung YC, Chiou JC, Tai SM, Chen HH and Huang GS. Nanosurface design of dental implant for improved cell growth and function. *Nanotechnology.* 2012 (IF: 3.652) revised

3. Pan HA, Hung YC, Sui YP, Huang GS. Topographic control of the growth and function of cardiomyoblast H9c2 cells using nanodot arrays. *Biomaterials.* 2012;33:20-8. (IF: 7.882)

4. Hung YC, Pan HA, Tai SM, Huang GS. A nanodevice for rapid modulation of proliferation, apoptosis, invasive ability, and cytoskeletal reorganization in cultured cells. *Lab Chip*. 2010;10:1189-98. (IF: 6.306)

5. Pan HA, Hung YC, Su CW, Tai SM, Chen CH, Ko FH, Huang GS. A nanodot array modulates cell adhesion and induces an apoptosis-like abnormality in NIH-3T3 cells. *Nanoscale Res Lett*. 2009;4:903-12. (IF: 2.894)

Patent:

1. 具有奈米結構的人工牙根(ARTIFICIAL TOOTH ROOT), Taiwan patent, Japan patent, and the United State patent, in press.

International conferences:

1. Hsu-An Pan, Yao-Ching Hung, Shih-Ming Tai, and G. Steve Huang, Application of Integrated Nanodevice to Obtain Optimal Nanotopography that Maximizes Proliferation and Mineralization of MG63 Osteoblasts, 6th World Congress on Biomechanics, Singapore, Aug. 2010. (Oral)
2. Yao-Ching Hung, Hsu-An Pan, Chia-Huei Lee, and G. Steve Huang, A Nanoplatform to Assist Clinical Diagnosis of Ovarian Cancer, Japan Society of Obstetrics and Gynecology, Japan, Apr. 2010.
3. Hsu-An Pan, Chia-Wei Su, G.S. Huang, Surface Nanotopography Influences

Implant Biocompatibility by Nanodot Arrays, International Conference on Neuroprosthetic Devices, Taiwan, Mar. 19-20, 2009.

4. Shih-Ming Tai, Hsu-An Pan, Yu-Ping Sui,Yao-Ching Hung, G.Steven Huang, Customized Nanodot Arrays Provide an Appropriate Platform for Neural Medical Device in Spinal Cord, International Conference on Neuroprosthetic Devices, Taiwan, Mar. 19-20, 2009.
5. Y.-P. Sui, H.-A. Pan, S.-M.Tai,Y.-C. Hung, G.-S. Huang, Nanostructured Electrode Surfaces Used for Implantable Neural Device to Improve Biocompatibility for Muscle Cell, International Conference on Neuroprosthetic Devices, Taiwan, Mar. 19-20, 2009.
6. Y.-C. Hung, L.-C. Huang, L.-M. Chen, Y.-Y. Chang, G.S. Huang, H.-A. Pan, M.-Y. Hong, Application of Nanodot Arrays to Evaluate The Invasion Potentials of Gynecological Cancer Cell Lines at Bio-Nano Interface, 12th Biennial Meeting of the International Gynecologic Cancer Society, Thailand, Oct. 2008.
7. H.-A. Pan, Y.-C. Hung, S.-M. Dai, M.-Y. Hong, G.S. Huang, A Nanodot Array Modulates Cell Adhesion and Induces an Apoptosis-like Abnormality in NIH-3T3 Cells, Japan Society of Obstetrics and Gynecology, Japan, Sep. 2008.